UNIVERSITÀ POLITECNICA DELLE MARCHE

FACOLTÀ DI INGEGNERIA

CORSO DI LAUREA IN INGEGNERIA EDILE-ARCHITETTURA

STUDIO DELLA STABILITÀ DEL PATRIMONIO CULTURALE DELLE SVALBARD SOTTO L'EFFETTO DEL RISCALDAMENTO GLOBALE

Stability of cultural heritage in Svalbard in a global warming

Relatore: Giuseppe Scarpelli

Tesi di laurea di: Noemi Pasquini

Correlatori: Anatoly Sinitsyn

Aleksey Shestov

A.A. 2022/2023

Acknowledgments

I would like to thank my UNIVPM supervisor, Giuseppe Scarpelli, for his guidance during this dissertation. Thanks to his availability and willingness to learn and research this new topic related to the Arctic. A deep thanks to my co-supervisors from SINTEF and UNIS, Anatoly Sinitsyn and Aleksey Shestov, who have sparked my passion for the study of structures in the Arctic soil, which has opened a new path in my academic journey.
Thanks to the universities UNIVPM, UNIS, NTNU, and the SINTEF institution for making this project and this experience possible.
Thanks to Anni Vehola, who has been a really good friend and colleague. Thanks for supporting each other and for sharing this experience with me.
Special appreciation goes to Professor David Scaradozzi, who consistently lent a helping hand during our virtual coffee meetings, offering guidance and support at every step of my international studies.

Grazie alla mia famiglia, che mi ha sempre supportato in tutte le mie scelte, anche quella di voler vivere nella cittá piú a Nord del mondo. Grazie per aver sempre creduto in me, perché senza il vostro aiuto tutti i successivi e precedenti ringraziamenti non sarebbero stati scritti.

Grazie ai a tutte le persone che hanno fatto parte della mia vita fino a questo momento, a tutti i miei amici che anche se lontani e in ogni parte del mondo sono sempre pronti a sostenermi e che quando ci rincontriamo è come se non fosse passato nemmeno un giorno.

Thanks to Svalbard. The place that made me feel at Home. Thanks to all the people I met here, I always felt I was, I am, in the right place.

The financial support for the fieldwork done in this thesis was obtained from the Arctic Field Grant project (RiS ID 11770), via the Research Council of Norway.

Prefazione

La storia delle Svalbard è relativamente breve, risalente a circa 600 anni fa ma il suo carattere storico distintivo è stato profondamente plasmato dal persistente patrimonio di strutture erette sui suoi paesaggi aridi e ghiacciati.

In particolare, all'interno di Longyearbyen e dintorni, una ricchezza di resti storici risale al periodo minerario, che rappresenta un patrimonio culturale di immenso significato per gli abitanti dell'Artico e quelli intimamente legati a questa regione polare. Questi impianti hanno svolto un ruolo chiave nel trasporto del carbone dalle miniere al porto commerciale per l'esportazione.

Ancora oggi, le attività minerarie persistono e la presenza duratura di impianti a fune dà ai minatori e alla comunità a loro interconnessa un profondo senso di continuità storica e di appartenenza al contesto Artico. Con il loro significato per lo sviluppo delle attività umane nell'Artico, i siti minerari riescono ad attrarre a Longyearbyen migliaia di turisti ogni anno e offrono occasione di studio e ricerca per la loro unicità. Si caratterizzano infatti perché "incastonate" nel permafrost, un terreno naturalmente ghiacciato che ricorda la roccia, e che aggiunge una dimensione distintiva al loro significato.

Tuttavia, la vulnerabilità del permafrost ai crescenti effetti del cambiamento climatico, con i conseguenti aumenti di temperatura e tendenze allo scioglimento, pone queste strutture storiche e le loro fondamenta a rischio considerevole di dissesti permanenti e, al limite, di collasso. Molte di queste strutture hanno già evidenziato sensibili cedimenti e perdita di verticalità, prefigurando un destino simile per molte altre. Di conseguenza, diventa imperativo un loro monitoraggio continuo e costante, e uno studio completo di queste strutture, tenendo conto delle variabili esterne, come nuovi ruscellamenti causati dal dissolvimento dei ghiacci, frane e sensibili aumenti degli afflussi di pioggia. È dunque fondamentale comprendere la vulnerabilità dei manufatti storici che caratterizzano l'Artico, se l'obbiettivo del nostro lavoro è quello di preservare e trasmettere la sua bellezza nel tempo.

Abstract

The history of Svalbard unfolds over a relatively short time span of approximately 600 years, yet its historical distinctive character has been profoundly shaped by the enduring legacy of the structures erected on its frigid landscapes.

Notably, within Longyearbyen and its surroundings, a wealth of historical remnants harkens back to the mining period, representing a cultural heritage of immense significance to the Arctic denizens and those intimately linked to this polar region. These structures played a pivotal role in transporting coal from the mines to the commercial port for exportation.

Still today, mining operations persist, and the enduring presence of cableway installations lends miners and their interconnected communities a profound sense of historical continuity within the Arctic. Moreover, these sites serve as a dual attraction: drawing thousands of tourists to Longyearbyen annually while also being an attraction for both study and research. Their unique construction atop permafrost, a naturally frozen ground that bears resemblance to bedrock, adds a distinctive dimension to their significance.

However, the vulnerability of permafrost to the growing effects of climate change, with its attendant temperature rises and melting tendencies, places these historic structures and their foundations at considerable risk of subsidence and structural compromise. Several have already experienced settlement and tilting, foreshadowing a similar fate for many others. Consequently, the imperative of continual monitoring and comprehensive study, factoring in external variables, is paramount to preserving and comprehending this invaluable Arctic.

Table of contents

Table of tables

Table of figures

Acronyms

MAT = Mean Air Temperature

MGST = Mean Ground Surface Temperature

MGT = Mean Ground Temperature at the depth of zero annual amplitude

ALT = Active Layer Thickness

MAAT = Mean Annual Temperature

DZAA = Depth of Zero Annual Amplitude

dGPS = differential GPS

1 Introduction

Since their discovery in 1596, Svalbard have been the scene of hunting, trapping, coal mining and scientific research activities. These different cultural heritage sites, such as hunting cabins, coal mines, and research stations, provide insight into the unique history of the island and its inhabitants. In Svalbard, monuments and sites older than 1946 are automatically protected [Svalbard's Environmental law]. The preservation and protection of these sites are important for telling the story of Svalbard's past and for fostering a sense of cultural identity among those who have a connection to the island. Cultural heritage sites are irreplaceable sources of historical information (Kathrine Nitter, 2022), which can indeed play a crucial role in the sustainable development of the Arctic region by serving as important markers of identity and attracting both locals and visitors. These sites have the potential to drive economic growth through tourism and provide educational opportunities, while also helping to preserve the cultural heritage of the region. The preservation and protection of cultural heritage sites are therefore crucial for ensuring a sustainable future for the Arctic and its people.

The rapid pace of climate change has made preservation and restoration strategies for cultural heritage sites increasingly necessary. Climate change can have significant impacts on cultural heritage sites, leading to physical degradation and loss of material due to degradation of permafrost, more frequent extreme weather events, and increased costal erosion. In order to protect these valuable cultural assets and ensure their survival for future generations, preservation and restoration strategies are essential. The archipelago of Svalbard is currently experiencing a rise in land elevation of approximately 2 millimeters per year relative to sea level as a result of glacial rebound. This has led to a local decrease in sea level in the region. Despite this decrease, there has been a corresponding increase in wave activity, which has raised concerns over the potential for elevated rates of coastal erosion.

These strategies include measures such as documentation, monitoring, physical protection, conservation and restoration work, risk assessment and management. Community engagement and education may be considered as future steps that may be useful for being included in the strategies. By taking proactive steps to protect cultural heritage sites, it is

possible to preserve the cultural and historical legacy of the Arctic and ensure that these sites continue to serve as markers of identity and attract visitors for years to come.

The project Polar Climate and Cultural Heritage – Preservation and Restoration Management is an important initiative in this regard, by being focused on the technical-industrial heritage of Longyearbyen and Ny-Ålesund. These former coal mining communities have large collections of technical-industrial heritage including buildings. The objective of this project is to provide a comprehensive set of recommendations for the management of cultural heritage sites in polar climates. To achieve this, we will produce high-resolution climate warming scenarios specifically tailored to the region of Svalbard. Furthermore, we will conduct a modelling of permafrost dynamics in order to develop risk-based engineering methods to evaluate the performance of foundations in permafrost. To ensure a holistic approach, we will also investigate sociological attitudes towards the preservation of cultural heritage. Lastly, we will provide input into the development of strategies for the preservation and restoration of cultural heritage sites in Svalbard. Through these multifaceted efforts, we aim to contribute significantly to the preservation of cultural heritage in this unique and vulnerable region.

The purpose of this thesis is to widen the knowledge related to the effect of climate change on foundations and foundation design in northern areas in permafrost subjected to seasonal effect of temperature changes, adapted (Instanes & Rongved, 2019).

The structures that make up the post cableway located in Longyearbyen (Svalbard) will be studied. Three of these structures will be taken as references to conduct the study: large, medium and small. The study aims to investigate the response of the foundations of these structures in relation to climate change and its effects on the surrounding environment and how this will be repeated on the same quotas.

This study focuses on the evaluation of structures´ foundations within the post cableway network situated in Longyearbyen, Svalbard. To conduct this investigation, three representative structures have been selected, and classified as big, medium, and small. The primary objective of this study is to explore how these structures' foundations respond to the impacts of climate change and its associated effects on the surrounding environment.

Figure 1.1 Big cableway post reference structure

Figure 1.2 Medium cableway post reference structure

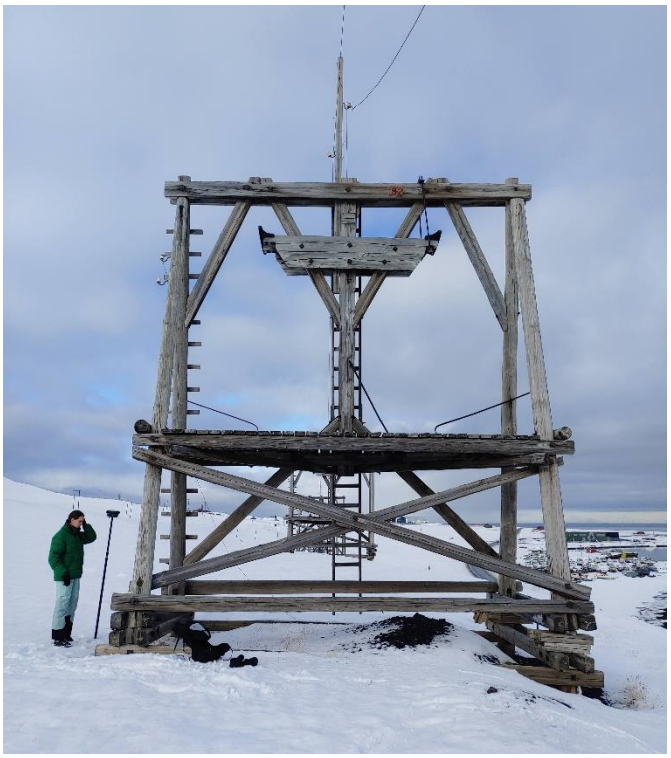

Figure 1.3 Small cableway post reference structure

2 Aims of the study

The primary goals of this thesis project encompass the following aspects:

- Investigating the impact of rising temperatures resulting from climate change on frozen soil.
- Analyzing how alterations in the thermal regime of the soil influence the settlement of the foundations which support the structures within the cableway post located in Longyearbyen.
- Assessing the anticipated retreat of the ice front in the coming decades (projected within the next 50-62 years), while taking into account the substantial penetration of the active layer observed so far.

3 Background

3.1 Frozen soil in the Northern Hemisphere

The frozen soil divides into two distinct parts: the perennial frozen part referred to as permafrost and the portion that seasonally freezes which is referred to as the active layer Figure 3.1. Permafrost areas consist of sediment or rock, along with ice and organic material, that remains at or below 0°C for at least two consecutive winters and the intervening summer(Orlando B. Andersland, 2003). Also, the mean annual temperature (MAAT) must be below 0°C to secure the existence of permafrost (Heller, 2021). Instead, the active layer is defined as the soil layer where the temperature fluctuates above and under 0°C and is where all the frost activity takes place (Nybo & Grimstad, 2017).

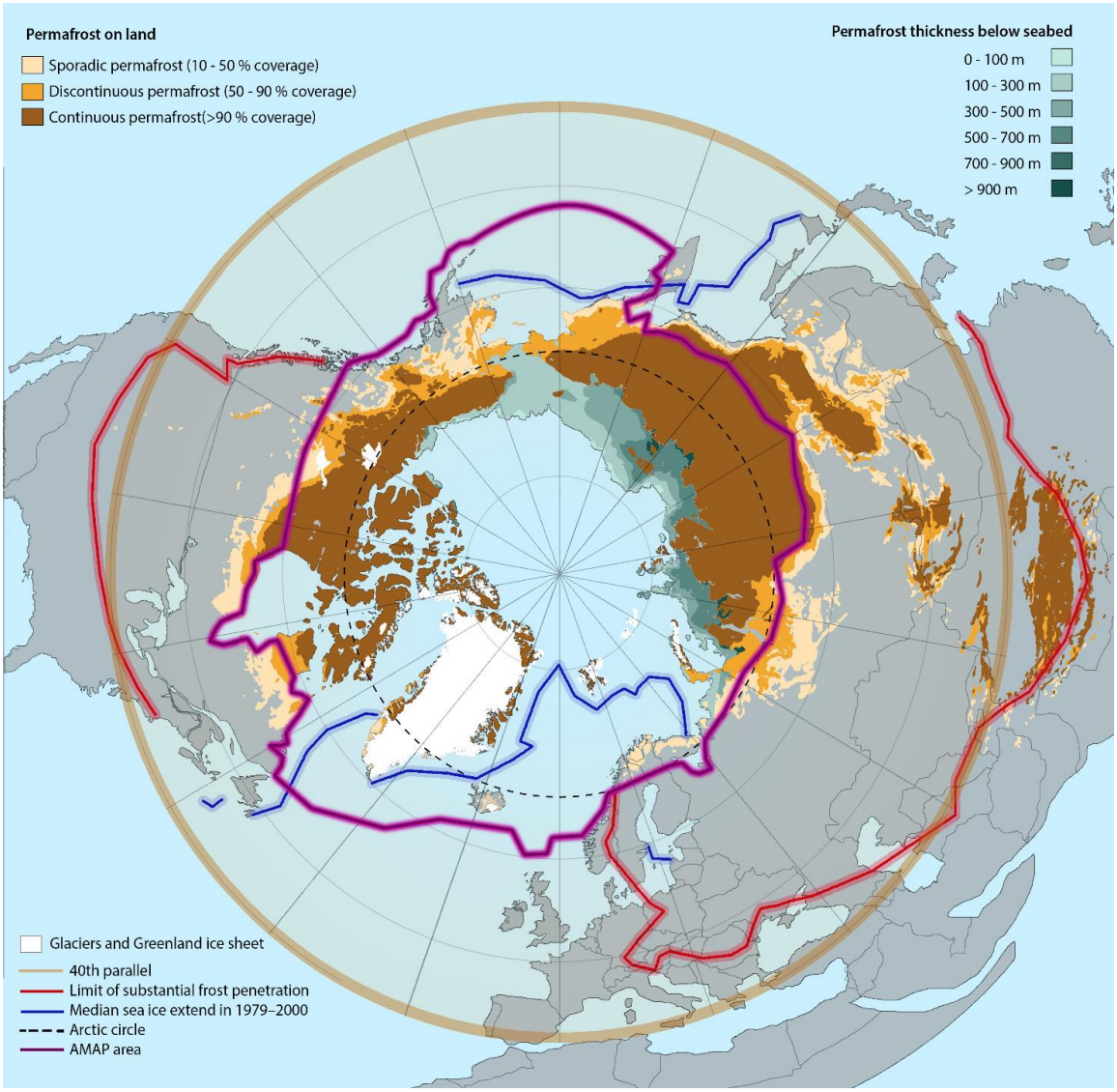

Figure 3.1 Seasonal frost and permafrost in the Northern hemisphere (Sinitsyn et al., 2020)

The Arctic region plays a crucial role in the global climate system, and the impacts of its changing climate can have far-reaching effects worldwide. It is undergoing rapid change when compared to other parts of the globe. The change is primarily driven by climate change and the effects on the cryosphere are substantial both at a local, national and regional scale (European Environment Agency, 2017). In the coming decades, the Arctic is expected to undergo significant transformation and as a result, the effects of this transformation are likely to become more pronounced over time (European Environment Agency, 2017). To further emphasize the significance of this issue, it is important to understand that the changing Arctic climate has the potential to impact the global climate system in several significant ways.

3.2 Svalbard archipelago

Svalbard is situated within the northern hemisphere and is characterized by a polar-tundra climate, as classified by the Köppen-Geiger system (Rouyet et al., 2019). The archipelago is within the Arctic Ocean, and it stretches between the 76° and the 81° parallel North. It covers 63000 km^2 where 60% of the total area is covered by glaciers, leaving to periglacial environment and permafrost (Huang, 2020).

The region is unique in that it has continuous permafrost, with varying thickness ranging from less than 100 meters in valley bottoms and coastal regions to more than 500 meters in mountainous areas. Variations in weather, both intra- and inter-annual, as well as local conditions such as water content, ground characteristics, snow cover, and vegetation, play a significant role in the permafrost and cannot be neglected in its analysis (Rouyet et al., 2019).

3.2.1 Permafrost in Svalbard

Svalbard has the warmest permafrost this far north in the Arctic (Hanssen-Bauer et al., 2018). The mean permafrost temperatures at 10–20-meter depth range from around -2.5°C in coastal western sites to approximately -5°C in central regions. Since 2009 the permafrost temperatures have increased at rates between 0.06°C and 0.15°C per year at 10 m depth (Hanssen-Bauer et al., 2018). The most reliable indicator of long-term changes in permafrost temperature is its measurement at the depth of zero annual amplitude (ZAA), where there is little to no fluctuation in the ground temperature. This depth varies from a few meters in warm, ice-rich permafrost to 20 m or more in cold permafrost and in bedrock (Hanssen-Bauer et al., 2018). To track changes related to permafrost in Svalbard, the "Climate in

Svalbard 2100" (Hanssen-Bauer et al., 2018) study, has identified permafrost temperature and active-layer thickness (the thickness of the layer that freezes and thaws annually over the permafrost) as the two essential climate variables (ECVs).

3.2.2 Active Layer

The layer of ground that is subject to annual thawing and freezing in areas underlain by permafrost.

COMMENT:

The active layer includes the uppermost part of the permafrost wherever either the *salinity* or clay content of the permafrost allows it to thaw and refreeze annually, even though the material remains cryotic ($T < 0°C$).

In Russian and Chinese literature, the term active layer covers two distinct types: (1) the *seasonally thawed layer* overlying permafrost, and (2) the *seasonally frozen layer* overlying *unfrozen ground* inside or outside permafrost areas (Van Everdingen, 1998).

The projected climate data show that temperatures will keep rising in Svalbard. Based on the analytical and numerical studies performed by SINTEF studies, for the projected temperature data, it is observed that the active layer thickness in Longyearbyen, will increase up to 2 m or more by 2100, depending on the thermal properties of the soil (Anatoly O. Sinitsyn, 2020). In fact, the active layer in Longyearbyen has been already observed to be increased by approximately 25-30cm since 1998 (Kristin Enevoldsen, 2022).

When the soil is thawing and freezing, the bearing capacity of the active layer changes during the seasons; and due to these seasonal changes, the strength of the active layer is unreliable, therefore its strength is neglected (Kristin Enevoldsen, 2022).

The active layer thickness depends on many factors, including the severity of winter temperatures (freezing index), soil and rock type, ground moisture content, snow cover, surface vegetation, drainage and the degree and orientation of slopes (Orlando B. Andersland, 2003).

3.2.3 Air temperature in Svalbard

The mean annual air temperature in Svalbard has increased between 3 ℃ and 5 ℃ during the last 40 to 50 years (L. Gilbert et al., 2019). According to a study on the Arctic SAT, which covers a period from 1981 to 2020, the increasing temperature rates for the Northern Barents Sea region are exceptional both for Arctic and global scale and correspond to 2 to 2.5 times the Arctic warming averages and 5 to 7 times the global warming averages (Isaksen et al., 2022).

3.3 Ground thermal regime

Air temperature influences the ground thermal regime in permafrost. The temperature of the air experiences fluctuations across various time scales, including daily, monthly, or yearly variations. These changes can be approximated as sinusoidal variations, which are then mirrored in the subsurface temperatures of the ground. Consequently, the temperature variation within the ground also exhibits a sinusoidal nature; however, its amplitude progressively diminishes with depth until reaching a point of equilibrium known as the depth of zero annual amplitude (DZAA). Adapted from (Heller, 2021).

The surface ground temperature ($T_{S,m}$) can be conveniently approximated as a sinusoidal fluctuation, which repeats on a daily and yearly basis. Equation (3.1) provides an estimation of the ground surface temperature using the observed data of the average annual ground temperature (T_m) and the amplitude of surface temperature variations (A_s) (Huang, 2020)

$$T_{S,m} = T_m + A_s \, sin \frac{2\pi t}{p} \tag{3.1}$$

where t is time, hours or days and p is the period expressed in days (365.25 days) (Figure 3.2).

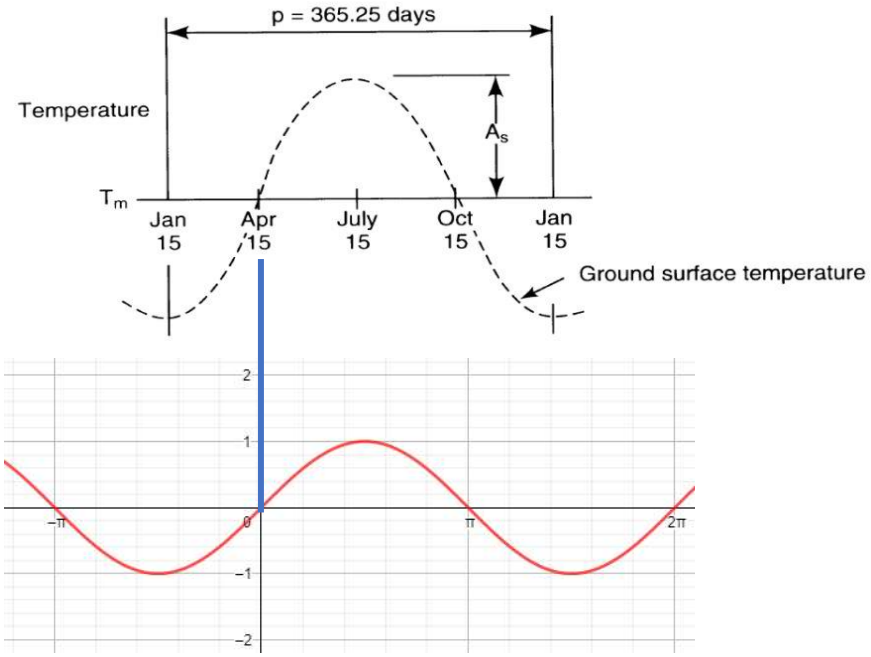

Figure 3.2 The variation on the ground surface temperature during a year (Orlando B. Andersland, 2003).

The range of annual ground temperature variations for any depth below the ground surface can be represented by a trumpet-curve (Orlando B. Andersland, 2003). A trumpet curve is shown in Figure 3.3, and is a plot of the warmest and coldest temperatures in the ground (through a year) (Instanes, 2016), see Equation (3.2).

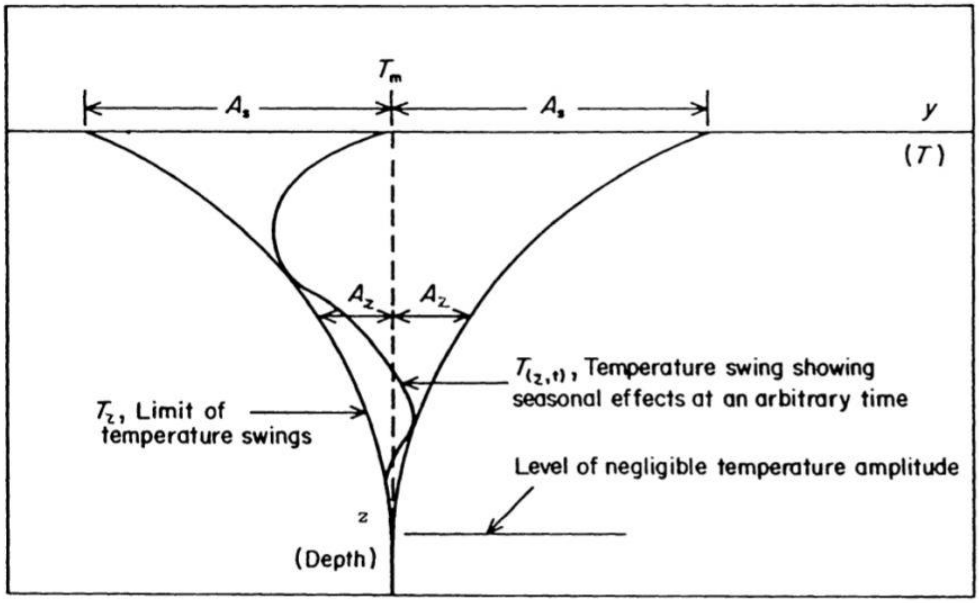

Figure 3.3 Temperature attenuation with depth (Orlando B. Andersland, 2003).

$$T_z = T_m \pm A_s \, exp\left(-z\sqrt{\frac{\pi}{\alpha_u p}}\right) \tag{3.2}$$

with symbols explained in Figure 3.3 and α_u is the thermal diffusivity, see (3.4).

In the permafrost foundation's design, the thermal criteria for the foundation's design are established by considering the warmest or maximum temperatures (T_{max}) in relation to the depth, as determined from the measured or computed trumpet curves. This approach involves calculating the maximum temperature experienced in the ground at various depths during the seasonal temperature variations. Adapt from (Instanes, 2016).

At a specific depth, the temperature exhibits a periodicity that matches that of the surface temperature, albeit with a reduced intensity and a time lag (Figure 3.4). As the depth increases, the magnitude of the time delay also increases, indicating that the temperature at greater depths takes longer to respond to changes in the surface temperature. The thermal conductivity of the material determines both the extent of the time delay and the amplitude of temperature variation at a given depth. The time delay refers to the duration required for the surface temperature to effectively heat up or cool down the soil until it reaches an equivalent temperature.

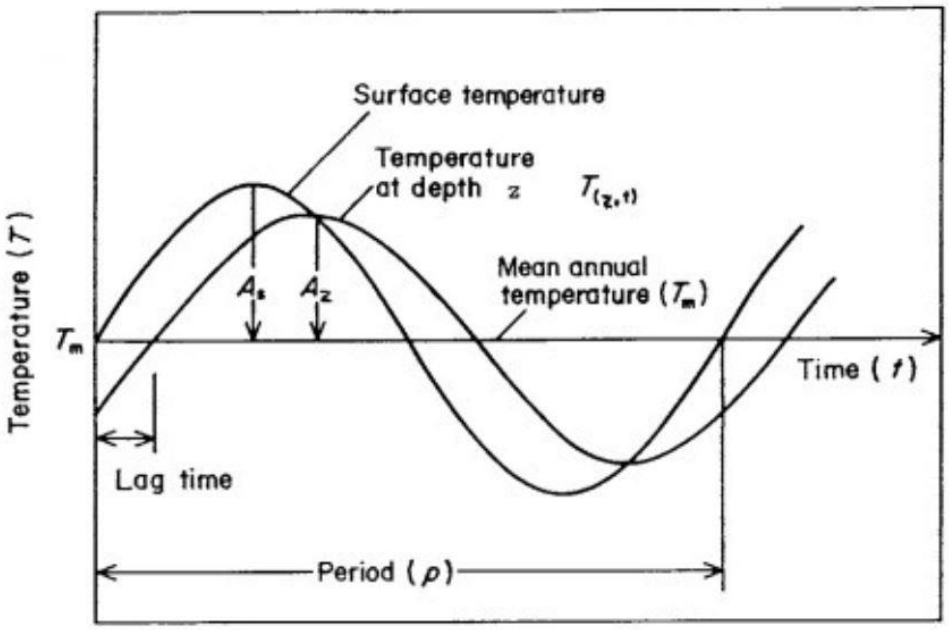

Figure 3.4 Simplified representation of the seasonal sinusoidal trend of air temperature and the grounds response showing the delay of the ground response to the surface temperature. Adapt from (Orlando B. Andersland, 2003).

Soil temperature profile: temperature vs time vs depth

At any time during the seasonal variation in temperature in the ground, the actual temperature at any depth and time, will lie between the boundaries of the trumpet curve (Instanes, 2016).

$$T_{z,t} = T_m + A_s \, exp\left(-z\sqrt{\frac{\pi}{\alpha_u p}}\right) sin\left(\frac{2\pi t}{p} - z\sqrt{\frac{\pi}{\alpha_u p}}\right) \quad (3.3)$$

3.4 Thermal properties

The response of soil materials to thermal changes requires an understanding of their thermal properties; thermal conductivity k, heat capacity c, thermal diffusivity α_u, and latent heat of fusion L (Orlando B. Andersland, 2003).

3.4.1 Thermal conductivity

The concept of thermal conductivity refers to the ability of a material to conduct heat. It measures the rate at which heat is transferred through the material. A higher thermal conductivity indicates that a material can transfer heat more efficiently. Adapt (Orlando B. Andersland, 2003). The thermal conductivity of permafrost can vary depending on factors such as its composition and moisture content. On average, the thermal conductivity of permafrost ranges from about 0.2 to 2.5 W/(m·K), with ice-rich permafrost having higher thermal conductivities compared to frozen organic-rich soils.

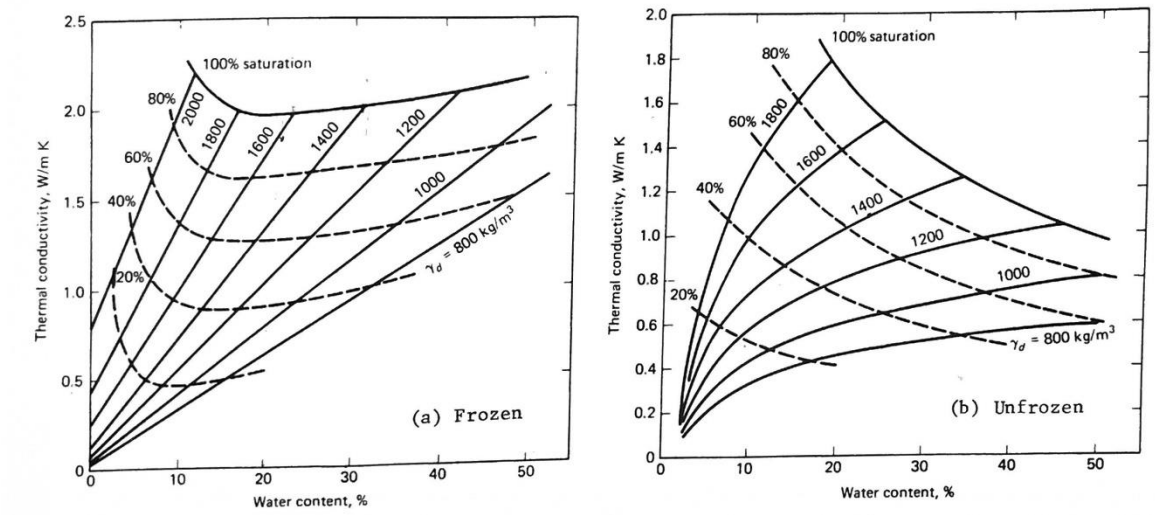

Figure 3.5 Average thermal conductivity for silt and clay soils: (a) frozen, (b) unfrozen (Orlando B. Andersland, 2003).

In fact, according to Mitchell et al., the denser a soil, the higher is its composite thermal conductivity, owing to the much higher thermal conductivity of the solids relative to the water and air. Furthermore, since water has a higher thermal conductivity than air, a wet soil has a higher thermal conductivity than a dry soil (Mitchell & Soga, 2005). Consequently, it can be inferred that ice-rich soil will exhibit even higher thermal conductivity, see Table 3.1.

Thermal Conductivity	Material	Btu/h/ft²/°F/ft	W/m/K
	Air	0.014	0.024
	Water	0.30	0.60
	Ice	1.30	2.25
	Snow		
	(100 kg m^{-3})	0.03	0.06
	(500 kg m^{-3})	0.34	0.59
	Shale	0.90	1.56
	Granite	1.60	2.76
	Concrete	1.0	1.8
	Copper	225	389
	Soil	0.15–1.5 (≈1.0)	0.25–2.5 (≈1.7)
	Polystyrene	0.015–0.035	0.03–0.06

Table 3.1 Material's thermal conductivity (Mitchell & Soga, 2005).

3.4.2 Heat capacity

The heat capacity c $[kJ/kgK]$ indicates the energy required to increase the temperature of one kilogram of material by one degree Celsius. For the same amount of supplied energy, materials with low heat capacity experience greater changes in temperature. The heat capacity of a material tends to rise as temperature increases. Additionally, an increase in density leads to an increase in the heat capacity of a given soil. Considering soils, as moisture content increases, the heat capacity also increases.

In fine-grained frozen soils (silt and clays), the liquid-solid phase change is gradual with a decrease in temperature (Orlando B. Andersland, 2003).

Heat Capacity	Material	Btu/lb/°F	kJ/kg/K
	Water	1.0	4.186
	Ice	0.5	2.093
	Snow		
	(100 kg m^{-3})	0.05	0.21
	(500 kg m^{-3})	0.25	1.05
	Minerals	0.17	0.710
	Rocks	0.20–0.55	0.80–2.20

Table 3.2 Materials' heat capacity (Mitchell & Soga, 2005).

When it comes to phase change systems or internal energy storage mechanisms, the heat capacity can vary depending on the temperature, pressure, soil structure, and composition. The apparent heat capacity takes into account these variations and provides an average or effective measure of the system's heat capacity under specific conditions.

3.4.3 Thermal diffusivity

In equations (3.2) and (3.3), α_u represents the soil thermal diffusivity. It quantifies the rate of heat transfer occurring within the soil mass. Equation (3.4) shows, that this rate is dependent on the thermal conductivity k, the bulk density of the soil mass ρ, and the soil heat capacity c (Orlando B. Andersland, 2003).

$$\alpha_u = \frac{k}{c\rho} \tag{3.4}$$

Typical values for thermal diffusivities, which are listed in Table 3.3, show that α_u for ice is much higher than that of water. For this reason, the diffusivity of frozen soil will be much higher than that of the same soil in the thawed condition (Orlando B. Andersland, 2003).

Material	Thermal diffusivity α_u $m^2/s \times 10^{-7}$	Source
Ice	11,2	Terzaghi 1952
Soft saturated clay	4	Terzaghi 1952
Dry soil	2,5	Terzaghi 1952
Water	1,4	Terzaghi 1952

Table 3.3 Materials' thermal diffusivity (Orlando B. Andersland, 2003).

3.4.4 Latent heat of fusion

The amount of heat energy absorbed when a unit mass of ice is converted into liquid at the melting point is defined as its latent heat of fusion (Orlando B. Andersland, 2003). The latent heat L of the soil is described by the following equation:

$$L = \rho_d L' \frac{w - w_u}{100} \tag{3.5}$$

where ρ_d is the dry density [kg/m^3] (Equation (*3.6*); L', is 333,7 kJ/kg, which represents the latent heat of fusion for water at 0 °C; w [%] the total water content and w_u [%] the unfrozen water content.

$$\rho_d = \frac{\rho_{bulk}}{1 + w} \tag{3.6}$$

3.5 Analytical solution

The distribution of temperatures in frozen soils, may be obtained by an analytical approach that aims to find a surface energy balance. In fact, the surface energy balance undergoes variations over different time scales, both annually and daily. Climatic factors, such as surface radiation, convective heat exchange between the air and ground, and heat flow resulting from evaporation or condensation, all influence the ground surface temperature (Heller, 2021). Unfortunately, detailed representations of the surface energy balance, are not often available, given the complexity of the calculations and the required time demand.

During some meetings with some experts, it was disclosed that certain studies conducted within SINTEF consider all the mentioned climatic factors. However, at present, these calculations are limited to specific long-term projects that have had ample time for data collection and analysis.

For these reasons, when insufficient site-specific data are available, the empirical-based n-factor approach is used to simulate the complex relation between air temperature and climate, adapted (Heller, 2021).

The seasonal surface n-factor is the ratio between surface and air freezing indexes (I_{sf}, I_{af}) or surface and thawing index (I_{st}, I_{at}) respectively, equations (3.7) and (3.8). The freezing index quantifies the accumulated cooling effect of sub-zero temperatures. It can be calculated by summarizing the mean temperature for days with temperature ($T < 0°C$) below 0° C over a winter season. The thawing index is the cumulative sum of the daily mean temperatures above 0°C ($T > 0°C$). It quantifies the accumulated warming effect of temperatures above freezing, indicating the extent and duration of thawing conditions. The indices are defined for the respective season by degree-days [°C · days].

The mathematical formulation of the surface n-factor can be expressed according to (Orlando B. Andersland, 2003):

$$n_f = \frac{I_{sf}}{I_{af}} \tag{3.7}$$

$$n_t = \frac{I_{st}}{I_{at}} \tag{3.8}$$

Freezing, thawing, and redistribution of water in the ground during seasonal temperature changes are responsible for variations in soil properties and the behavior of foundation materials. The depth to which these materials are affected requires prediction of the seasonal frost penetration (Orlando B. Andersland, 2003).

For this purpose, the Stephan equation, equation (3.9), is a fundamental mathematical expression used to model the rate of heat transfer within the ground. It helps predict the growth and retreat of the active layer, which is the upper portion of the ground that experiences seasonal thawing and freezing. The equation takes into account various factors, the soil thermal conductivity (k), the absolute value of surface freezing (I_{sf}), and the latent heat of fusion (L). This information is essential for understanding the response of permafrost to changing climatic conditions and their potential impacts on infrastructure, ecosystems, and land stability.

$$X = \sqrt{\frac{2 \cdot k \cdot I_{st}}{L}} \tag{3.9}$$

However, it is important to acknowledge that Stephan's equation is a simplified model that may not account for all complexities and heterogeneities present in real-world permafrost systems. Farther, in the thesis, the outcomes derived from this equation will be compared with empirical data, numerical analyses of subsurface temperatures, and analytical ground temperature simulations conducted using Temp/W software. Furthermore, this thesis will mostly consider the thawing depth (X_t), as the primary focus lies in studying the most severe climate scenario characterized by rising temperatures.

3.6 Mechanical properties

Frozen soil is a natural particulate composite, made of four different constituents: solid grains, ice, unfrozen water, and gases (Orlando B. Andersland, 2003). Frozen ground occurs when the temperature of soil or rock drops below the freezing point, causing the pore water to turn into ice. Frozen ground can have a significant impact on the stability and integrity of structures, as well as on the movement of water and other fluids through the soil.

The overall strength of soil with ice depends on various factors, including the soil type, ice content, the orientation of the ice crystals, and the applied load. A comprehensive evaluation of the soil's strength properties is necessary to determine its overall resistance. The strength of ice increases with decreasing temperature, and its mode of failure is strain-rate dependent (Y. Zhang et al., 2022).

3.6.1 Hydrostatic pressure effect on frozen soil behavior

The behavior of frozen soil under an increase of hydrostatic pressure is considered to be the result of combined mechanical and thermodynamic effects, the former governing the stress sharing, and the latter the pressure melting phenomena (Orlando B. Andersland, 2003). When a granular material is frozen and then subjected to hydrostatic confining pressure, the pressure causes local melting to occur at the points where the grains come into contact with each other. This is because the pressure increases the temperature at these contact points, causing the frozen material to thaw. As a result of this local melting, water migrates towards regions of lower stress within the material. This migration occurs because the water seeks to reduce the overall stress on the system by flowing towards areas of lower stress. This behavior is known as "pressure melting".

If the confining pressures are very high, so that the grain structures collapse, a total pressure melting of the pore ice will occur even in dense sand (Orlando B. Andersland, 2003).

Hydraulic conductivity refers to the ability of a soil or rock to transmit water through its pores and fissures. In the case of frozen soils, the hydraulic conductivity for water is limited but not entirely absent, as stated by(Orlando B. Andersland, 2003), this means that water can still flow through the soil, although at a much slower rate than in unfrozen soils.

Unfrozen water

An important characteristic of frozen natural soil is that even though it exists below the freezing point of pure bulk water, not all the water is necessarily frozen (Orlando B. Andersland, 2003).

Despite the presence of unfrozen water, when ice fills most of the pore space, the mechanical behavior of the frozen soil closely reflects that of ice. This means that the soil's strength, density, and other properties will be similar to those of the ice. However, the soil will be more susceptible to freezing and thawing cycles, which can cause damage to structures built on it. In fact, frozen soils that contain a considerable amount of unfrozen water, may produce excess pore-water pressure under eternal loas, especially at temperatures near the thawing point (H. Zhang et al., 2020) and the variation of the pressure has a capability in influencing the deformation of frozen soils (H. Zhang et al., 2020).

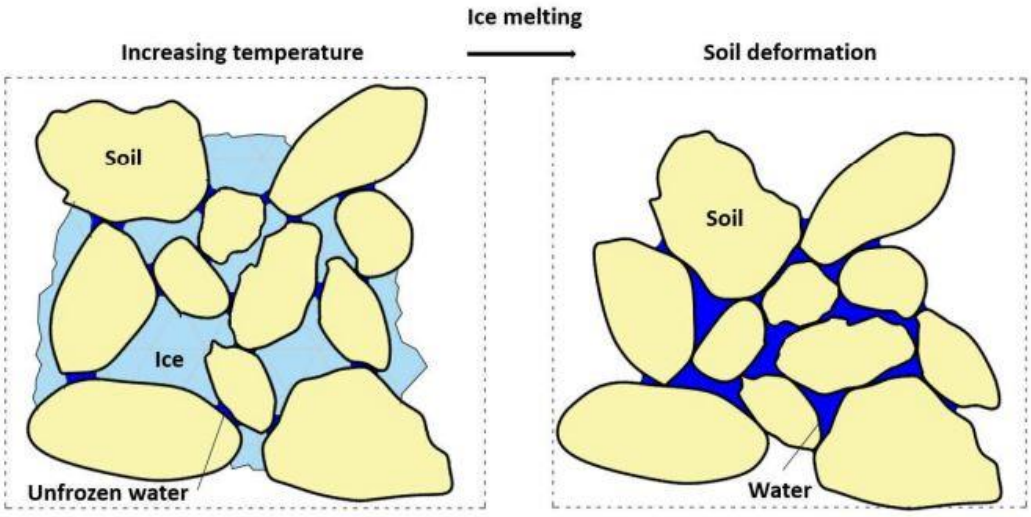

Figure 3.6 Schematic representation of, a) frozen soil, and b) thawed soil (with associated volume change) (Shastri et al., 2021).

When a load is applied to a frozen soil specimen, it exhibits two types of deformation: instantaneous deformation and time-dependent deformation. The former, thus the reversable component, determines the response of frozen soils to very-short-term and dynamic loads (Orlando B. Andersland, 2003); the latter, known as creep, refers to the gradual deformation that occurs under a constant applied stress. Understanding the distinction between these two deformation behaviors is crucial in comprehending the mechanical response of frozen soil under load. The type of deformation that occurs depends on the soil's properties, the loading conditions, and the time frame over which the loading occurs.

In the case of ice-saturated frozen soil under an increase in stress containing a substantial deviatoric component, the soil will show an instantaneous response, adapted from (Orlando B. Andersland, 2003). The soil will behave as an elastic material and will experience an immediate deformation in response to the applied loads.

Soil stress has both hydrostatic and deviatoric components, the first refers to the uniform stresses of the soil in all directions, while the second refers to the stress differences with directions. In the case of ice-saturated frozen soil, the deviatoric component of the stress can cause cracking or fracturing in the soil, which can further affect the soil's behavior.

3.6.2 Strength of frozen soils

This section discusses the mechanical behavior of a representative frozen soil sample. The focal point here is the concept of resistance, denoted as σ_{fu}, which is derived from a creep model. Sigma depends on several influential factors, notably the strain rate and temperature. In the context of strain rate, it's important to note that rapid compression of the material yields higher resistance in contrast to slow compression, leading to the onset of creep phenomena. Likewise, temperature exerts a significant influence on σ_{fu}, as it directly correlates with the deformation of the frozen soil samples. Permafrost deformability increases with temperature. Equation (3.10) introduces a temperature ratio, delineating the relationship between the temperature at the foundation depth and a reference temperature. The temperature exponent, denoted as "w", in this context, must be smaller than 1, ensuring that as the exponent increases, the absolute value of the power decreases.

σ_{fu} represents the level of stress that determines the change in the behavior of the sample material, specifically in the context of this thesis focused on frozen soil samples that eventually undergo rupture. It considers the stress level that leads to system failure, serving as the foundation for calculating the bearing capacity.

$$\sigma_{fu} = \sigma_{c0}\left(1 + \frac{\theta}{\theta_c}\right)^{w}\left(\frac{\varepsilon_f}{\dot{\varepsilon}_c t_f}\right)^{\frac{1}{n}} \tag{3.10}$$

Where σ_{c0}, θ_c, w, ε_f, $\dot{\varepsilon}_c$, and n are held constant.

θ_c is the reference temperature and its value is 1°C; w is the temperature exponent ≤ 1; ε_f equal to 0,1 is the failure strain corresponding to the strain at the minimum creep rate; $\dot{\varepsilon}_c$ equal to 10^{-5} hours is the reference strain rate for ice-rich silt; n is the creep exponent for

stress; and σ_{c0} is the reference stress at $\dot{\varepsilon}_c$ when θ tends to 0°C; and t_f is the time frame considered.

In light of this, in this study constant stress and variable temperature will be considered.

The specific value of "w" would depend on the material and the physical processes at play. For frozen soil, a smaller "w" might represent the fact that frozen soil can become significantly more deformable with relatively small changes in temperature. On the other hand, the creep exponent "1/n" characterizes how a material's mechanical properties evolve with temperature. A reduced '1/n' value could indicate that frozen soil becomes increasingly responsive as temperatures rise.

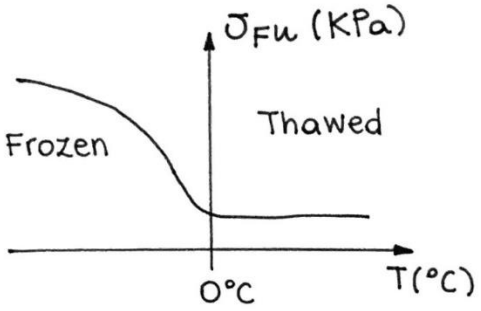

Figure 3.7 Schematic soil strength variation with temperature change, adapted (Orlando B. Andersland, 2003).

3.6.3 Total stresses analysis and bearing capacity of shallow foundations

In unfrozen soils, the allowable pressure for a shallow foundation is usually based on safety against general soil failure and on the tolerable foundation settlement, adapted (Instans Arne, 2017). Similar criteria are also applicable to shallow foundations in frozen soils, but here the strength of such soils is temperature dependent, and the main source of foundation settlements is deviatoric creep rather than consolidation (Orlando B. Andersland, 2003).

The bearing capacity can be calculated as follows:

$$q_{ult} = p_o N_q + c N_c s_c d_c i_c b_c g_c \tag{3.11}$$

where s_c represents the shape factors; d_c represents the depth factors; i_c represents the inclination factors; b_c represents the inclination under the foundation factors; g_c represents the inclination at ground level factors; N_q is the bearing capacity factor related to the angle of internal friction of the soil, it quantifies the soil's shear strength and its ability to resist

deformation under load; and N_c is the bearing capacity factor related to the cohesion of the soil.

The soil's cohesion and the soil load due to soil weight around the foundation can be determined through the follow equations:

$$c = \frac{\sigma_{fu}}{2}$$

|(3.12)

$$p_o = \gamma_{bulk\_ground} \cdot D$$

(3.13)

where D is the foundation depth, see also Figure 3.8 .

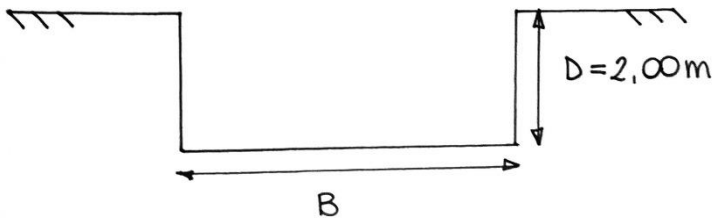

Figure 3.8 Section of the foundation excavation.

Safety factor

The safety factor represents a critical parameter in engineering, serving as a quantitative measure of the margin of safety between the applied load and the capacity of a structure or material to withstand such loads. The safety factor assumes significance by quantifying the level of safeguard against potential ground failure resulting from imposed loads.

The safe or allowable soil pressure is defined as:

$$q_a = \frac{q_{ult}}{F_s}$$

(3.14)

3.6.4 Creep of frozen soil

When studying creep in frozen soils, researchers often conduct laboratory experiments using specialized equipment that allows for the application of constant stress over an extended period. The deformation of the soil sample is measured over time to observe the creep response.

Strain – time

The creep strain-time curve is one of the common graphs used to illustrate the creep behavior of a frozen soil. This curve plots the cumulative strain (deformation) of the soil sample over time under constant stress. Initially, the curve shows a rapid deformation phase, known as primary creep, where the strain increases rapidly (
Figure 3.9 a). After the primary creep, frozen soils often enter a relatively stable phase called steady-state creep. In this stage, the strain increases at a constant rate over time under the sustained applied stress (
Figure 3.9 b). The strain-time graph during steady-state creep shows a linear relationship, with a constant slope representing the steady-state creep rate of the frozen soil.

For low stress levels, ice-poor soils will display only primary creep and will asymptotically approach some limiting deformation; instead, ice-rich silts and clays exhibit an abbreviated primary creep period and a prolonged secondary creep stage, while tertiary creep, may never be attained (Orlando B. Andersland, 2003).

In laboratory tests, the applied pressure is typically kept constant or determined based on specific test objectives and conditions. Similarly, the boundary conditions are often controlled to simulate the wanted scenario. However, it's important to note that in real-world situations, frozen soils can exhibit different behaviors under varying conditions. Factors such as changes in stress levels or temperature can trigger a transition from the stable creep state to a phenomenon known as accelerated creep. In these circumstances, the time-dependent deformation of frozen soils can experience a significant increase, surpassing the creep rate observed under steady conditions. This transition to accelerated creep highlights the sensitivity of frozen soils to external factors and emphasizes the need to consider dynamic changes in stress and temperature when assessing their long-term behavior. The strain-time graph during accelerated creep exhibits a steeper slope, reflecting the faster accumulation of strain over time. If the stress applied to the frozen soil exceeds its strength capacity or

adverse environmental conditions occur, the strain-time graph may show a sudden and significant increase in strain, indicating failure (
Figure 3.9 c). Failure in frozen soils can manifest as shear failure, tensile failure, or a combination of both, depending on the soil properties and stress conditions.

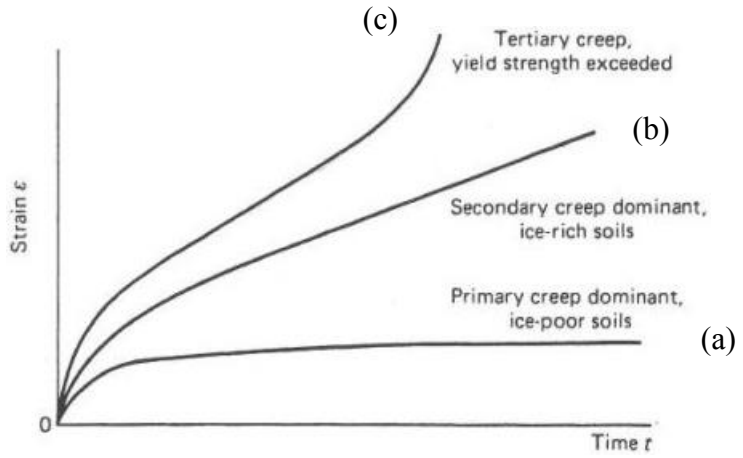

Figure 3.9 Strain – time graph (Orlando B. Andersland, 2003).

For step loading under uniaxial stress conditions and constant temperature, the creep behavior exhibited by frozen soils, along with many other materials, is often characterized by a specific type of creep curve, as depicted in Figure 2.7. This curve serves as a valuable tool to understand the time-dependent deformation response of frozen soils (Orlando B. Andersland, 2003)).

Figure 3.9 illustrates a typical creep curve that is commonly observed in medium- to high-density ice-saturated sands and silts (Orlando B. Andersland, 2003). These materials, when subjected to sustained stress, display a distinct creep behavior. This representation provides insight into the progressive deformation of frozen soils and their sensitivity to sustained stress. It highlights the importance of considering the creep behavior when analyzing the long-term stability and deformation characteristics of structures built on frozen ground.

The creep curves depicted in Figure 3.10 and Figure 3.11 provide insights into the relationship between strain and strain rate in frozen soils as they evolve over time. There curves offer a visual representation of how the strain and the strain rate are interconnected during the creep process.

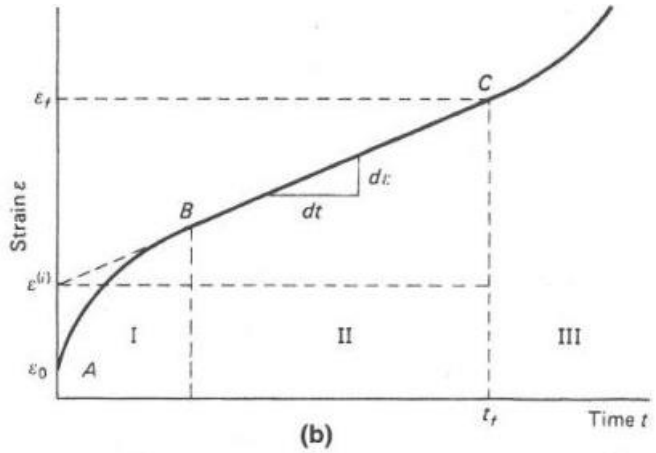

Figure 3.10 Basic creep curve (Orlando B. Andersland, 2003). The curve represents the ratio of the change in shape or size of a material in response to an applied stress.

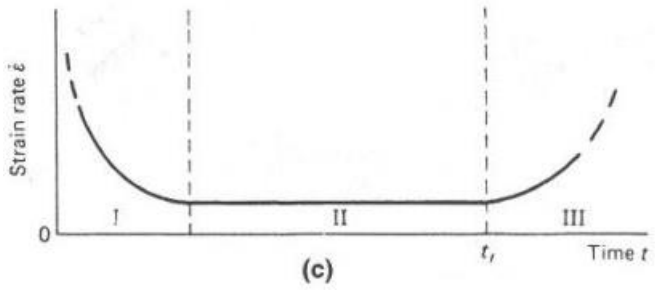

Figure 3.11 Strain rate versus time (Orlando B. Andersland, 2003). The curve quantifies the speed of the deformation process; how quickly the material s deforming or undergoing a change in shape.

3.7 Settlement analysis of shallow foundations

The authentic solution settles due to three mechanisms:

- Settlement in unfrozen ground below the foundation.
- Melt of ice in the ground below the foundation
- Creep of the frozen ground below the foundation

3.7.1 Elastic settlement

The settlement of unfrozen soil as a result of the compression of the active layer is defined as:

$$s = I(1 - v^2)\frac{pB}{E} \tag{3.15}$$

where I is the influence factor; v is the Poisson's ratio, usually taken as 0,35 for drained conditions (see Table 3.4); p is the pressure at foundation level; B is the width of the foundation; and E is the soil modulus of deformation (Jean-Lous Briaud, 2013).

Silt	Modulus E (MPa)	Poisson's ratio v
Soft silt	4 – 8	0,3 – 0,35

Table 3.4 Modulus and Poisson's ratio values for silt (Jean-Lous Briaud, 2013).

3.7.2 Consolidation

Volume change of thawing soil will result from both phase change (ice to water) and flow of excess water out of the soil (Orlando B. Andersland, 2003). The following equation denotes the subsidence resulting from the thawing of ice within the soil beneath the foundation:

$$\delta_{melt} = \Delta h \cdot n \cdot 0{,}1 \tag{3.16}$$

where Δh is the variation in active layer thickness between the two years marking the extremities of the desired time span under examination; n is the porosity of the soil, which is assumed to be frozen and fully saturated; and $0{,}1$ represents the decrease in volume of 10% when the ice melts.

$$n = 1 - \frac{\rho_d}{\rho_s} \tag{3.17}$$

where ρ_d is the soil dry density and ρ_s the solid density. These values are assigned as 1600 kg/m^3 and 2650 kg/m^3 respectively.

Jean-Lous Briaud, 2013, states that this part of the settlement process accounts a time-delayed component associated with water stress dissipation. In fact, the hypothesis made is that every summer, the active layer experiences a slightly deeper thaw than the previous year, and that in winter it completely refreezes. Consequently, with the complete saturation of pores, due to ice, the melting process is attributed not only to the increase in air temperatures during seasonal changes but also to the influence of pore pressure.

3.7.3 Creep settlement

Creep settlement refers to the gradual deformation of a material under a sustained load over time. The following equation serves as a tool for quantifying and modeling the complex interplay of factors influencing creep settlement. By dissecting this equation, we can unveil the relationship between applied stress, time, material properties, and historical loading conditions.

Frozen soil type	b	n	w	σ_{c0} [kPa]
Suffield clay	0.33	2.38	1.2	170
Bat-Baioss clay	0.45	2.50	0.97	180
Hanover silt	0.15	2.04	0.87	2250
Callovian loam	0.37	3.70	0.89	310
Ice-rich silt	1.00	3.00	0.60	71
Ottawa sand	0.45	1.28	1.00	1050
Manchester fine sand	0.63	2.63	1.00	160
Karlsruhe silty sand	0.40	2.00	1.00	300
Very ice-rich soil or polycrystalline ice	1.00	3.00	0.37	1030

Table 3.5 Creep parameters determined from laboratory tests. From (Orlando B. Andersland, 2003).

$$s = aI \cdot \left(\frac{q}{\sigma_{c\theta}}\right)^n \left(\frac{\dot{\varepsilon}_c \cdot t}{b}\right)^b \tag{3.18}$$

where a is the width B of the foundation divided by two; q is the vertical pressure i.e. the weight of the structure and the weight of the soil above the foundation; n is the creep exponent for stress, a parameter that describes how sensitive the creep settlement is to changes in stress. It characterizes the non-linearity of the creep behavior.; b is creep

exponent for time, $b = 1$, steady-state creep, w is the temperature exponent ≤ 1; t the time and $\dot{\varepsilon}_c$ is the reference strain rate (10^{-5} hour);

$$\sigma_{c\theta} = \sigma_{c0}(1 + \theta)^w$$

(3.19)

where: $\sigma_{c0} \rightarrow$ reference stress at $\dot{\varepsilon}_c$ when θ tends to 0°C, which is the stress level at which the material has fully consolidated and no longer undergoes significant volume change.

The influence factor for rectangular footings is defined as:

$$I = I_{st}\left(1 + \left(\frac{I_c}{I_{st}} - 1\right)\frac{B}{L}\right)$$

(3.20)

where I_c and I_{st} are calculated as follows.

Influence factor for circular footings:

$$I_c = \left(\frac{3}{2n}\right)^n$$

(3.21)

Influence factor for strip footings:

$$I_{st} = \left(\pi\frac{\sqrt{3}}{4}\right)\left(\frac{\sqrt{3}}{n}\right)^n$$

(3.22)

3.8 Climate change effects on Svalbard's frozen soil

Given the ongoing trend of climate change, the long-term stability of permafrost in Svalbard is a matter of concern. The region has experienced a continuous warming trend since the 1980s, raising concerns about the durability, in terms of preservation, stability and settlements of infrastructure built on permafrost (Instanes & Rongved, 2019). An increase in ground temperatures in permafrost regions may reduce the bearing capacity and increase settlement rates and subsidence of foundations, and stability of natural and engineered slopes (Instanes & Rongved, 2019). Climate change impacts the properties and distribution of frozen ground and changes of the ground thermal regime can modify the distribution, magnitude and timing of ground heave, subsidence and creep (Rouyet et al., 2019). This highlights the importance of acquiring knowledge related to these impacts in order to effectively address the challenges posed by climate change on the preservation of cultural heritage in Arctic regions.

Figure 3.12 visually depict the consequences of rising temperatures, a direct outcome of global warming. It is well-established that the Arctic region is experiencing the impacts of climate change at an accelerated pace, approximately four times faster than many other parts of the world. Within this context, our study examines the ramifications on permafrost.
For instance, in 2020, certain regions exhibited an active layer with a depth of 2.00 meters. However, when projecting ahead to 2050, it becomes evident that the ice front could recede by an additional 50 cm. This alarming trend has the potential to instigate the formation of taliks, both at the surface and subsurface levels. Such occurrences not only have critical implications for environmental stability but also significantly amplify the risks associated with building and infrastructure instability.

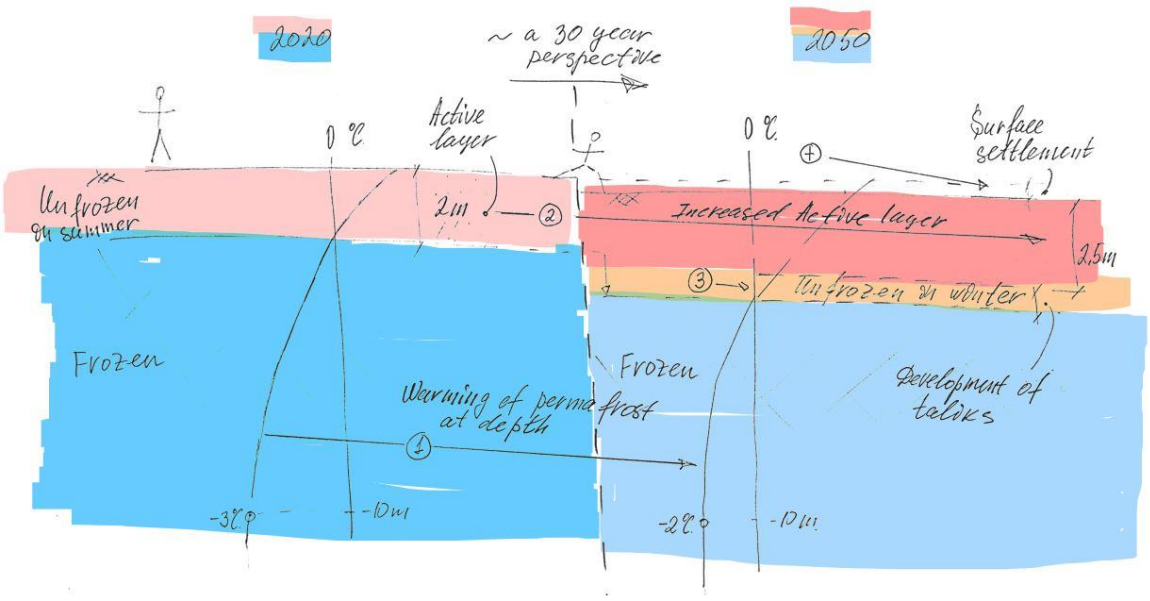

Figure 3.12 Impacts of global warming – degradation of permafrost (Anatoly O. Sinitsyn).

4 Methodology

This chapter presents the methodology to study the thermal regime of the ground and data collection to achieve the objective of the study, namely, to calculate the settlement of the cableway post's foundations. At the outset, a diverse range of analytical methods to assess the soil's thermal regime are employed; followed by a transition into the geotechnical domain, where field-acquired data come into play. Firstly, numerical analysis methods are introduced, which are the basis of numerical simulation in this study. Following, observed data are listed. Subsequently, the mathematical formulation at the base of the chosen numerical software GeoStudio TEMP/W is introduced. Ultimately, forecasts regarding the soil's thermal regime are made, providing valuable insights into the anticipated changes in frozen ground conditions around Longyearbyen, while simultaneously paving the way for new research inquiries in the future.

4.1 Design of shallow foundations

Design procedures used for footings involve the following steps:

1. Select the footing depth, in this case the foundation depth is give, due to are existing structures.
2. Estimate the warmest temperatures below the footing for determining relevant soil properties (see Section 4.2 Thermal analysis).
3. Select the footing size from bearing capacity theory with the prescribed factor of safety.
4. Carry out a settlement analysis using the appropriate constitutive relationship for the foundation soil.
5. Modify the footing size or depth when settlements or settlement rates are to be excessive.

4.2 Thermal analysis

The thermal analysis in this master thesis relies on the Orlando B. and Andersland method as well as Stephan's equations. Both analytical approaches use historical temperature data. To determine the specific years used in calculating the soil's thermal behaviour, we employed a process involving the computation of melting indices (as described in section 4.2.1.1). As stated by Orlando B. Andersland, 2003, the standard design index, in this case, is defined as the average air thawing index of the three warmest summers during the most recent 30 years of record. These two methods are employed for calculating the Active Layer Thickness (ALT), with the aim of illustrating that they yield different results due to the consideration of different factors in their calculations. Furthermore, the first method provides insights into temperature trends, which are not accessible through the second method.

Subsequently, the collected data underwent thorough analysis. These datasets originated from boreholes strategically positioned in various locations encompassing Longyearbyen and its vicinity. The initial dataset was sourced from the University Center of Svalbard, which, in 2017, deployed thermal strings on the outside eastern side of the university campus. To visualize the real trends in soil temperature and accurately determine the thickness of the active layer of permafrost, we plotted this data using an Excel worksheet application.

Furthermore, supplementary real-world data were acquired from “Climate in Svalbard 2100” (Hanssen-Bauer et al., 2018). This source, rather than providing time-series data, offered a compilation of active layer measurements for different years and locations. These locations were then presented in Figure 4.1, corresponding to points labelled 3 and 4.

The third approach employed for estimating the Active Layer Thickness (ALT) is fully numerical, with the use of the Temp/W software, a finite element solution of the thermal problem for soils.

4.2.1 Finite element analysis with GeoStudio Temp/W

TEMP/W is a powerful finite element software product for modelling heat transfer and phase change in porous media (GeoStudio). TEMP/W can analyse simple conduction problems to complex surface energy simulations with cyclical freeze-thaw, like the changing seasons. The software provides a finite element solution of conduction, forced convection, and phase change in soils (GeoStudio). This makes TEMP/W a suitable tool to study various real-world

situation, such as understanding how permafrost responds to climate change, or assessing how man-made structures affect the temperature in the ground, adapted (GeoStudio).
One of TEMP/W's features is the ability to account the energy associated with the phase change (water turning into ice and vice versa), adapted (GeoStudio). The rate at which the latent heat is absorbed or released is controlled by an unfrozen water content function. Above the phase change temperature, all the water is unfrozen. As the temperature falls below the phase change point, the portion of the water that remains unfrozen decreases (GeoStudio).

4.2.1.1 Boundary conditions

Boundary conditions can be applied in form of functions or constants (Heller, 2021). In this project functions of temperature fluctuation will be used. Initially, observed data will be employed, followed by the incorporation of forecasted data at a later stage. In this context only thermal boundary conditions are relevant, adapted (Heller, 2021). Additionally, the introduction of forcing data into the model will take the form of a spline function.

4.2.1.2 Materials' definition

The primary objective of this research is to develop an exhaustive comprehension of the behavior of frozen ground under particular conditions, particularly within the context of climate change and the associated temperature increases. The focus of this investigation lies in the analysis of silt as the chosen soil material. Existing data from the chosen literature have been employed to establish the key soil parameters and properties pertinent to frozen silt. These critical parameters encompass aspects such as thermal conductivity in both frozen and unfrozen states, phase change temperature, volumetric water content, and volumetric heat capacity.
The conversion from gravimetric water content to volumetric measurements is done by the implementation of Equation (4.4). Likewise, the determination of heat capacity in volumetric units is accomplished by applying Equations (4.2) and (4.3), which specifically pertain to volumetric heat capacity in frozen and unfrozen states, respectively.

$$c_{Vu} = \frac{\rho_d}{\rho_w}\left(0{,}17 + 1\frac{w}{100}\right)c_{Vw} \tag{4.1}$$

$$c_{Vf} = \frac{\rho_d}{\rho_w}\left(0{,}17 + 1\frac{w_u}{100} + 0{,}5\frac{w - w_u}{100}\right)c_{Vw}$$

(4.2)

where w is the water content, $w_u$is the unfrozen water content, c_{Vw} is the water volumetric heat capacity equal to 4,187 MJ/m^3, from (Orlando B. Andersland, 2003), ρ_d is the dry density of the soil, ρ_w is the water density.

$$w = \frac{m_w}{m_s}$$

(4.3)

$$\theta = \frac{V_w}{V} = \frac{m_w \rho_{bulk}}{\rho_w m} = \frac{\rho_{bulk}}{\rho_w} \cdot \frac{m_w}{\frac{m_w}{w} + m_w} = \frac{\rho_{bulk}}{\rho_w} \cdot \frac{w}{1 + w}$$

(4.4)

Having defined these material properties, they are subsequently applied uniformly throughout the entire study region. Adopting a uniform soil model aims to facilitate a comprehensive examination of the material's behavior across the entire research area, providing valuable insights into its response to various changing climate conditions.

4.2.1.3 Geometry and mesh

TEMP/W mesh is fully automatic, handles complex geometries and ensures mesh compatibility on regions. Before generating the mesh you must specify the size of the global element. Regional alterations of the element are possible by specifying the number of divisions along one edge. In addition, it is recommended that the mesh structure is chosen in a similar way to the geometry and that it meets the type of data that will be entered, adapted (Heller, 2021).

4.2.1.4 Verification and validation of the model

After setting all the parameters, the focus shifts towards the verification and validation of the model. The objective here is to ascertain whether the model exhibits the desired response. This involves executing the model while inputting surface temperature data derived from observed measurements and set them into the surface boundary conditions.

Once the model is executed, the data generated by the model is exported to Excel and compared with the real data collected from the borehole. If correspondence between the data is found, the next step involves importing the forecasted data. This calibration process ensures that the model aligns more closely with the real-world conditions at the outset.

Following this step, an interconnected derivative model, linked to the original, is generated, and new boundary conditions are applied at the surface. Utilizing forecasted temperature data, a new design iteration is initiated.
This phase of the research is important for assessing the dynamic temperature fluctuations within the soil. By inputting forecasted data, the model is employed to simulate and analyze how soil temperatures are expected to evolve over time, shedding light on the complex temporal patterns and responses within the soil system under study.

4.4 Geotechnical analysis

The geotechnical analysis pertains to the foundations of structures constituting the Longyearbyen cableway system. Specifically, this analysis focuses on three selected structures, each representing one category, high and dimension related, within the cableway system. The analysis is structured into three distinct phases, beginning with the fieldwork phase. During this initial stage, data and pertinent information concerning the selected structures are directly gathered.

Subsequently, the second phase involves the evaluation of the ground's bearing capacity. This phase aims to assess whether the ground can adequately support the loads imposed by the selected structures.

The third phase comes into play only if the results from the second phase indicate that the ground's bearing capacity is sufficient. In such cases, this phase involves a settlement analysis.

4.4.1 Data collection: Fieldwork

In order to carry out the geotechnical analysis within the scope of this master's thesis, extensive fieldwork was undertaken, necessitating the acquisition of data directly from the structures under investigation. These field measurements primarily focused on gathering information regarding the dimensions of these structures, to estimate both their height and the resultant load they exert on the underlying foundation soil. However, the attainment of precise calculations proved challenging due to the inherent difficulties in accessing these structures.

Initially, consideration was given to employing laser-based measurement techniques to ascertain the height of these structures. Nonetheless, this approach was found to be impractical due to the considerable height and uneven contours of some of these structures. Additionally, alternative digital measurement tools could not be utilized during the data collection phase, which happened in March 2023, due to their inability to withstand the harsh low-temperature typical of the region during that period of the year.

Consequently, a more pragmatic approach was adopted, entailing the utilization of draft of drawings (see Figure 4.1 and

Figure 4.2) and pictures, which shows more details of the structures. Furthermore, measurements were conducted on the structures themselves, albeit partially, due to limited access.

During these site visits, base beams' dimensions measurements were taken, the inclinations of oblique beams were recorded, and measurements between successive steps on the staircase-like elements that traverse these structures from their base to their apex were obtained. Additionally, the thickness of these stair-like components was measured. Through the application of field measurements and trigonometric principles, the dimensions of the three distinct categories of structures, namely big, medium, and small, were determined. It is worth noting that while structures within each category exhibited variations in terms of beam count and height, efforts were made to select representative specimens that best characterized their respective categories.

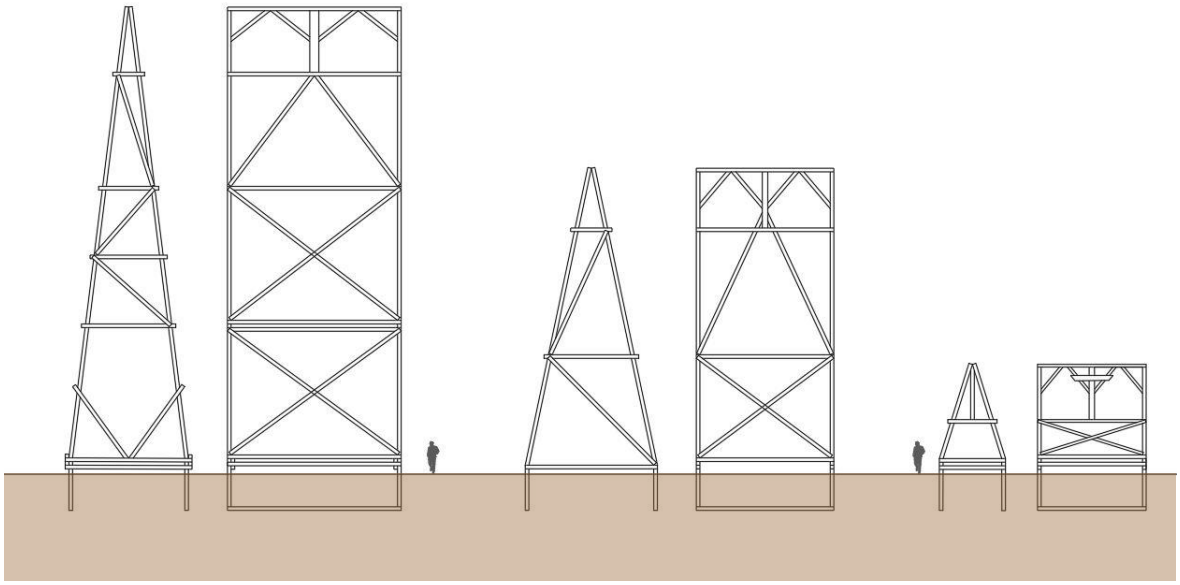

Figure 4.1 Cableway post structures: big, medium and small. Designed Using AutoCAD. Two human figures have been incorporated to provide a visual reference for the scale of these structures, with each figure standing at approximately 1.80 meters in height.

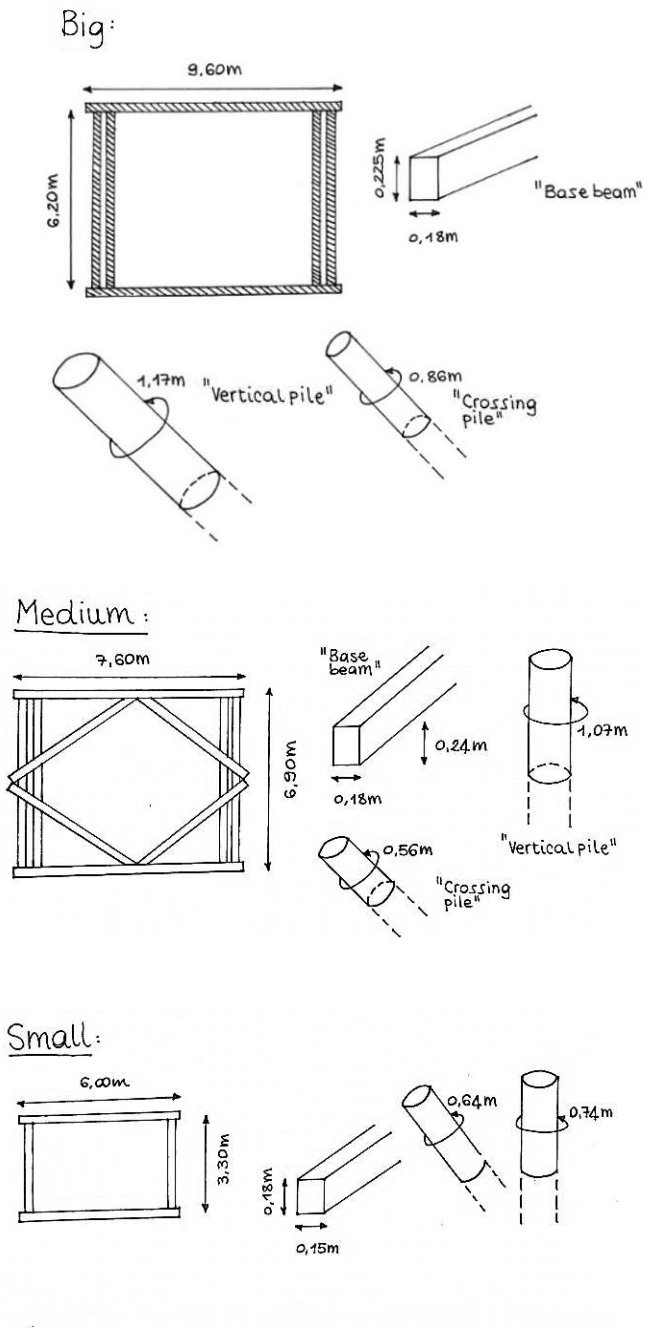

Figure 4.2 Cableway tower base skatches from fieldwork: big, medium and small structure

Figure 4.3 Cableway post, in winter and summer, rispectively in the fist and second picture.

4.4.2 Bearing capacity verification

By applying (3.11), a comprehensive assessment of the bearing capacity in terms of total stress for the three cableway post structure – big, medium, and small – has been carried out, while concurrently establishing an a priori safety factor that will subsequently undergo a validation process.

Typically, when dealing with frozen soils, there are usually no significant challenges in verifying bearing capacity. This is because, as long as foundations are partially embedded in frozen soil, the risk of general failure of the underlying soil is minimal. Addressing this, in his paper titled "Coastal Permafrost-Foundation Design Incorporating Climate Warming Scenarios," Instans Arne underscores the prevailing assumption within the field that bearing capacity analysis for frozen soils yields satisfactory safety margins against foundation failure, and the focus is then shifted to the accumulated strain during the service lifetime of the structure.

4.4.3 Settlement verification and performance criteria

The settlement of shallow foundations can be comprehensively understood as the sum of three distinct components, namely elastic settlement, consolidation, and creep settlement. These three individual facets collectively contribute to the overall settlement behaviour of shallow foundations and represent key areas of investigation within the realm of geotechnical engineering and foundation design research.

The requirement for the foundation depth is that the foundation should be placed at a sufficient depth to avoid thawing under the base of the foundation during the service life time of the structure It is also advantageous to avoid load application on the surface soil layers that may contain organic matter (Instans Arne, 2017)

Acceptable deformations or settlement is of course dependent on the structure’s sensitivity to (differential) settlements (Instans Arne, 2017). When evaluating the performance of foundations in ice-rich permafrost subjected to 30 years of load application, certain settlement thresholds have been established. According to Instans Arne's findings in 2017, a foundation settlement of less than 5 cm after this period is categorized as "good" from a design perspective. If the settlement remains below 10 cm, it falls within the "acceptable" range. However, if the settlement exceeds 10 cm, this is indicative of a foundation performance issue and is deemed a "failure" within the context of the foundation's structural integrity in ice-rich permafrost conditions. These delineated settlement limits serve as a

crucial benchmark for evaluating the effectiveness and stability of foundations in such challenging environments, which will be a focal point of investigation in this master's thesis.

5 Data analysis and results

Meteorological data for a given location are used to provide the mean annual temperature (T_m) and the surface temperature amplitude (A_s) (Orlando B. Andersland, 2003).

5.1 Soil parameters

The soil parameters are calculated according to the equations presented in chapter 2, section 2.4 Thermal properties. If the unfrozen water content w_u is assumed equal to zero and the silty soil is assumed fully saturated, the calculations yield the soil parameters presented in Table 5.1.

Soil	c [kJ/kg/K]	ρ [kg/m^3]	ρ_{bulk} [kg/m^3]	k_f [W/mK]	k_t [W/mK]	α_u [m^2/s]	L [J/m^3]
Silt	2,20	1600	2000	2,00	1,60	3,33e^{-7}	133480000

Table 5.1 Thermal and physical properties of frozen silty soil, when unfrozen water is assumed to be zero.

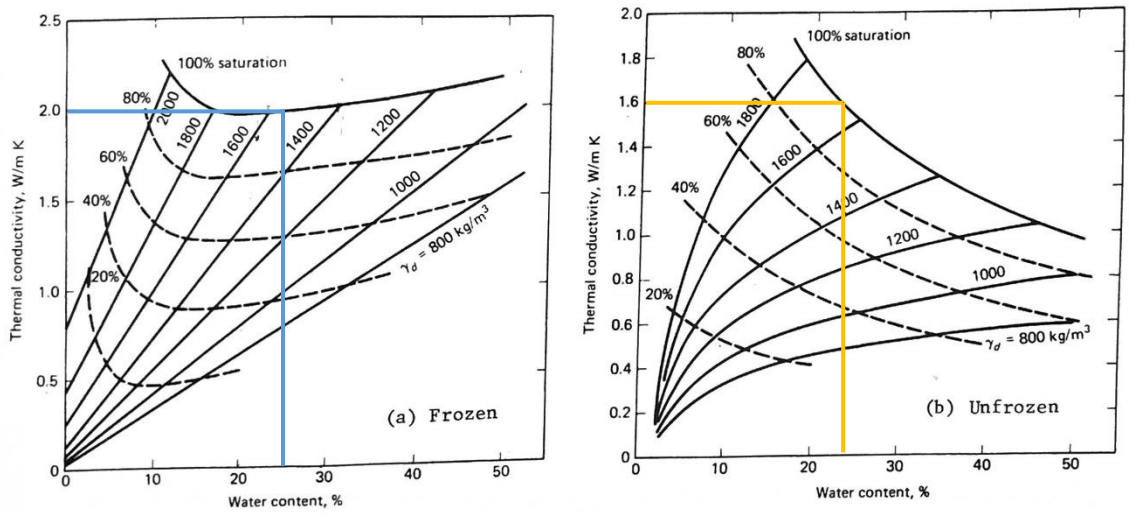

Figure 5.1 Thermal conductivity for (a) unfrozen and (b) unfrozen silt with a water content of 25%, adapted from (Orlando B. Andersland, 2003).

5.2 Project Overview

The aim of the thesis is to determine the settlements of some specific structures within the cableway post in Longyearbyen. These structures hold cultural heritage significance, due to they have been built before 1946. For this reason, they are legally protected according to Sysselmesteren's regulations. The calculations are carried out by considering the effects of climate change. The rate of climate change in the Arctic is observed to be at least four times faster than the global average. Hence, this study takes into account the accelerated climate change in the Arctic, while evaluating its effects on the cableway post structures'.

The project consists of two main parts, one concerning the thermal aspect and the other the geotechnical aspect.

5.2.1 Thermal analysis

In this first part, the soil temperature oscillations at different depths are studied. This study involves a comparison of the calculated Active Layer Thickness (ALT) with different approaches and datasets, including analytical, direct observations, and numerical calculations.

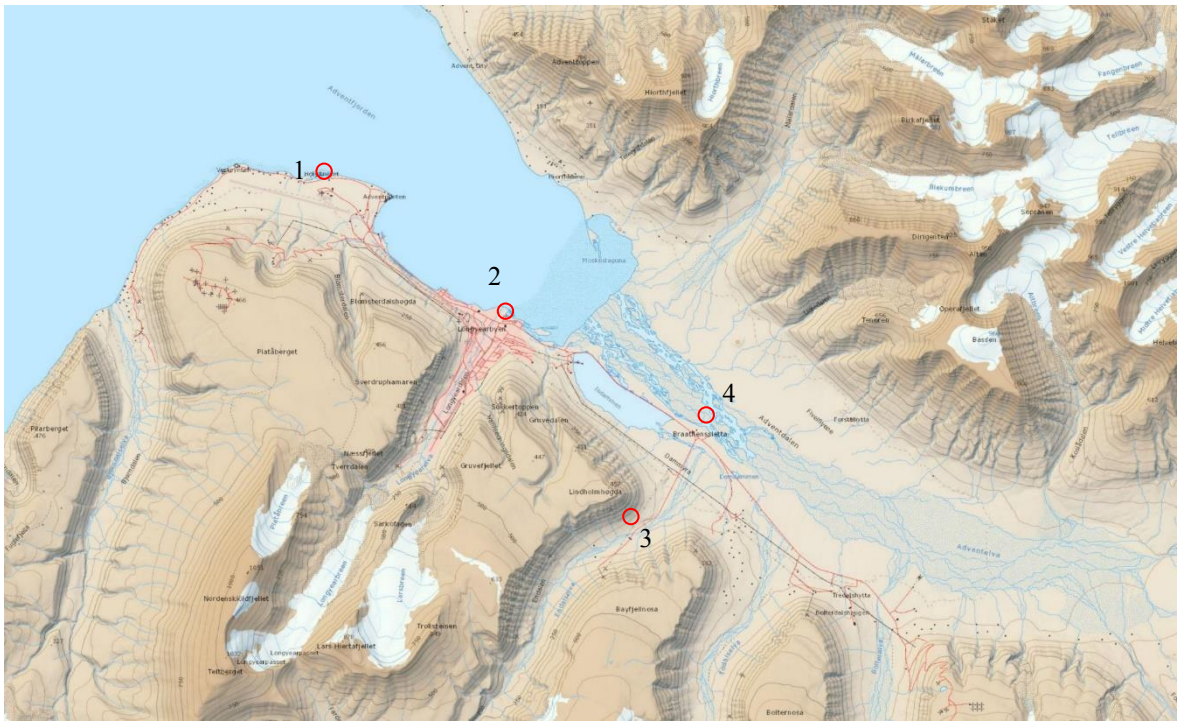

Figure 5.2 Data collection locations

1. Airport
2. UNIS East side
3. Old Aurora Station 2
4. Endalen

5.2.1.1 Results from analytical calculations

Two analyses have been performed. The first one employs the method proposed by Orlando B. Andersland, 2003, while the second utilizes Stephen's equation. Both methods have been previously described in section 2.3. In these two methods, historical temperature data sets from the Norwegian Meteorological Institute (MET) spanning the last 30 years, from 1992 to 2022, were considered.

5.2.1.2 Orlando B. and Andersland method

The research focused on the identification of the three warmest years by calculating the thawing indexes for the given period, as presented in Table 5.2. Consequently, the years with the most significant melting rates were determined to be 2016, 2020, and 2022. Respectively:

2016: I_t = 937,9 degree-days

2020: I_t = 860,2 degree-days

2022: I_t = 920,2 degree-days

Year	I_t	I_f	Missing data
1992	524,5	-2375,7	1
1993	602,5	-2818,3	0
1994	401,8	-2552,1	0
1995	569,2	-2759,7	0
1996	478,3	-2252,4	0
1997	464,1	-2642,9	0
1998	596,5	-2818,6	0
1999	550,7	-1949,8	0
2000	565,1	-2013,6	1
2001	642,8	-2302,2	0
2002	681,9	-2230,7	0
2003	586,3	-2806,8	0
2004	601,7	-2160,1	1
2005	669,5	-1743,3	0
2006	770,4	-1363,8	0
2007	697,2	-1609,2	0
2008	578,2	-2015	1
2009	631	-1971,4	0
2010	594,7	-2089,1	0
2011	752,7	-1962	0
2012	646,8	-1360,5	1
2013	725,2	-1980,2	-8
2014	673,1	-1426,2	-3
2015	668,7	-1463,4	-14
2016	937,9	-902,3	-17
2017	770	-1524,6	-5
2018	740,4	-1387,8	0
2019	695,7	-1934,3	-4
2020	860,2	-2083,8	-3

2021	527,6	-1575,3	-28
2022	920,2	-1748,7	-1

Table 5.2 Summary of the thawing and freezing index of the last 30 years, from 1992 to 2022. The fourth column indicates the number of days of missing data. The three warmest years are highlighted in light yellow. In Figure 5.3 are shown Trumpet curves estimated for the three warmest years.

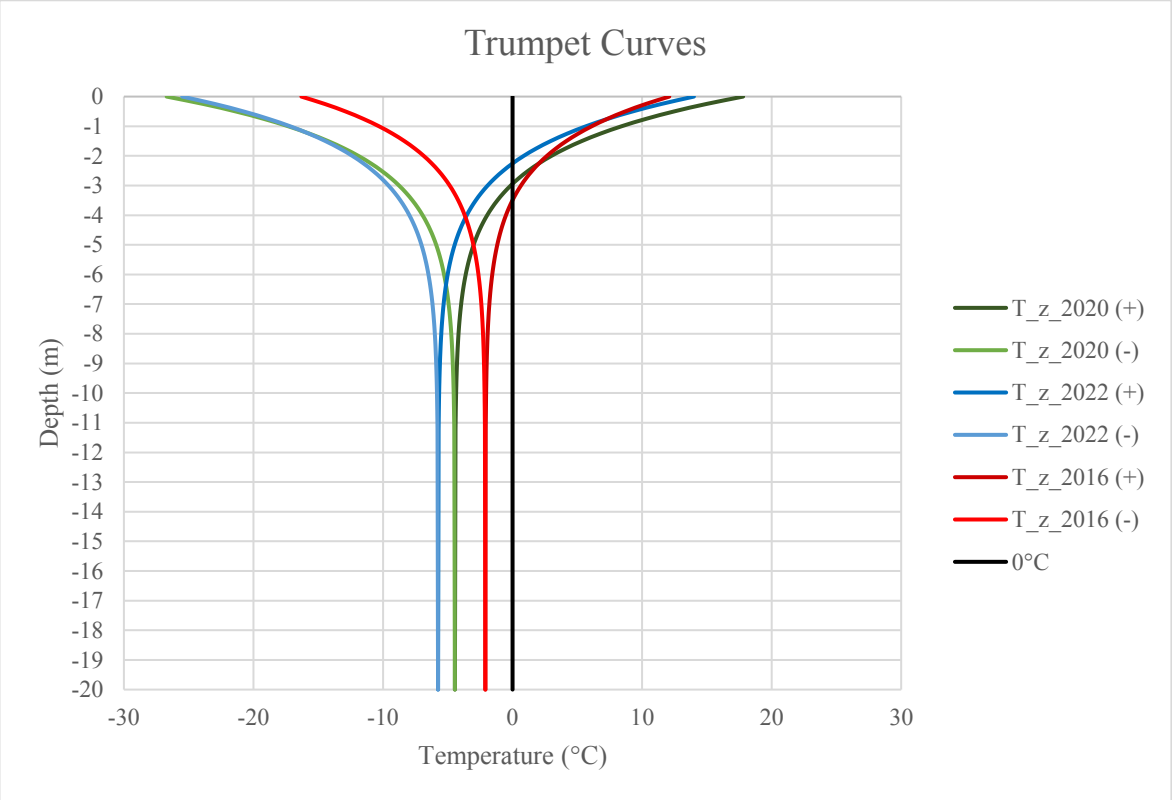

Figure 5.3 Trumpet curves for the three warmest years of the last 30 years

The depths obtained with this method are the following:

ALT 2016: 3,50 m

ALT 2020: 3,00 m

ALT 2022: 2,25 m

This depth will be reached in September 2016 and October for both 2020 and 2022.

5.2.1.3 Stephan's equation method

After identifying the three warmest years through the thawing indexes, the respectively surface thawing factors are calculated with Equation (3.8), Table 5.3. Afterwards, Equation (3.9) is used to calculate the thawing depth (X).

Material	n – factor $_{freezing}$	n – factor $_{thawing}$
Sand and gravel	0,9	2,0

Table 5.3 Sand and gravel n – factors (Orlando B. Andersland, 2003).

Year	I $_{thawing}$ (°C days)	I $_{surface\ thawing}$ (°C days)	I $_{surface\ thawing}$ (°C sec)
2016	937,9	1875,8	162069120
2020	860,2	1720,4	148642560
2022	920,2	1840,4	159010560

Table 5.4 Thawing indexes

The depths obtained with this method are the following:

ALT 2016: 2,20 m

ALT 2020: 2,11 m

ALT 2022: 2,18 m

5.2.1.4 Observed data

The ground temperatures reflect the air temperatures with exponential dampening with depth and a time lag. This means that the maximum thaw depth (active layer thickness) is observed on a later date than the maximum surface temperature (Instanes & Rongved, 2019).

The observed data come from different sources and places in Longyearbyen and its surroundings. The first dataset to be introduced pertains to thermos strings installed by the University Center of Svalbard behind Logistics. The collection of these data started in 2017. The second datasets are from different locations in Adventdalen and data from the years 2016 – 17 and 2008 – 09 have been reported.

5.2.1.5 Data from UNIS thermistor-strings

The thermistor-string placed in the borehole has been collecting data since 2017. Consequently, conducting a soil temperature comparison for the warmest year (2016) becomes unfeasible. The same holds true for the year 2022, as an extensive dearth of data prevents any meaningful comparison.

Instead, data from the year 2020 are at our disposal, and they reveal that the maximum active layer thickness is recorded in the month of September, see Graph 5.1:

ALT 2020: 1,00 m

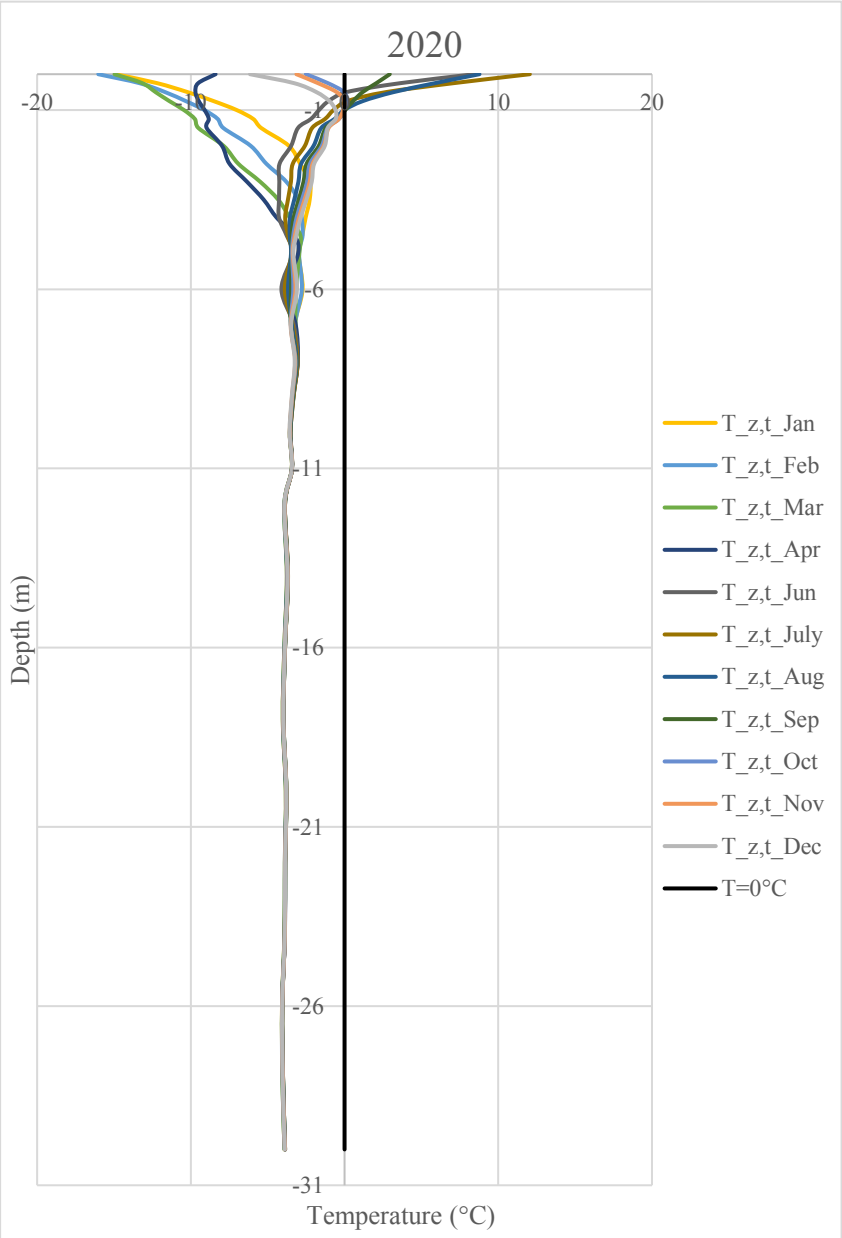

Graph 5.1 Ground temperature envelopes in the soil profile at the UNIS East side in 2020. Data from May have been removed, due to they did not look correct.

5.2.1.6 Data from Hanssen-Bauer et al., 2018

To address the data gap for the year 2016, information from the "Climate in Svalbard 2100" dataset has been incorporated. The region around Longyearbyen is notably responsive to warming trends, adapted (Hanssen-Bauer et al., 2018). The permafrost temperature records nearby the town generally show a continuous temperature increase in the upper 10-20 m of the ground the last 20 years. Since 2008-2009 ground temperatures have increased with rates between 0.06°C and 0.15°C per year at 10 m depth (Hanssen-Bauer et al., 2018).

		2016-2017				2008-2009	
Location	Borehole name/ID	MAT (°C)	MGST (°C)	MGT (°C)	ALT (°C)	MGT (°C)	ALT (°C)
Adventdalen	Old Aurora Station 2	-1,9	-1,3	-5,2 (9,9 m)	94	-5,6 (9,9 m)	90
	Endalen	-1,9		-2,7 (19 m)	190	-3,2 (15 m)	120
	Breinosa	-3,8	-4,1	-5,1 (10 m)	49	n/a	n/a

Table 5.5 Permafrost monitoring sites, ALT for the years 2008-2009 and 2016-2017 (Hanssen-Bauer et al., 2018).

MAT = Mean Air Temperature

MGST = Mean Ground Surface Temperature

MGT = Mean Ground Temperature at the depth of zero annual amplitude

ALT = Active Layer Thickness

5.2.1.7 Numerical calculation with Temp/W

The simulation aims to show the evaluation of the ground temperatures in the active layer and the permafrost, based on the predicted temperature data. To demonstrate this, the thermal analyses are performed from the periods 2018-2021 and from 2022-2080, adapted (Kristin Enevoldsen, 2022).

Model geometry and mesh definition

A rectangular soil sample characterized by a width of 10,00 meters and depth of 40,00 meters has been created as a 2D model, as shown in Figure 5.4.

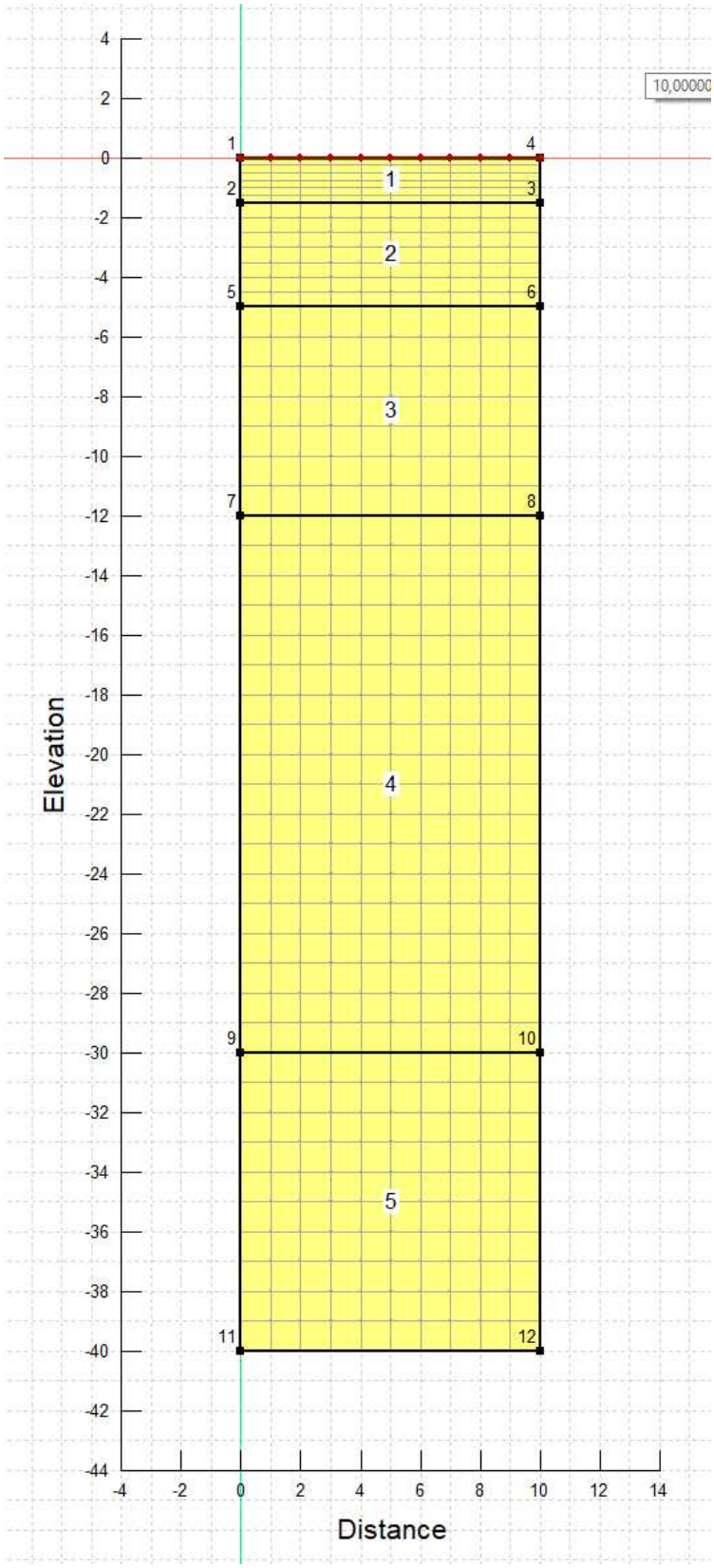

Figure 5.4 Model geometry and mesh used for the representative thermal analysis, where X re the x-axis represent the width and the y-axis denotes the depth.

Material properties definition

A full thermal model is used to model the thermal properties in Temp/W, the adopted soil parameters are presented in Table 5.6. The model assumes a uniform silty soil composition, with the thermal conductivity (k) being incorporated as a spline data point function.

	Parameters	Value
Thermal conductivity	k_f = constant	2,00 W/mK
	k_u = constant	1,60 W/mK
Volumetric heat capacity	c_f = constant	1 976 kJ/m^3/°C
	c_u = constant	2 813 kJ/m^3/°C
Volumetric water content	w	0,40

Table 5.6 Definition of soil material parameters for a simple thermal model in Temp/W

Initial and boundary conditions definition

The spatial function for the initial temperature profile on January 1, 2018, is established based on the initial measured temperatures obtained from the UNIS-EAST side borehole. These initial configurations are visualized in Figure 5.7.

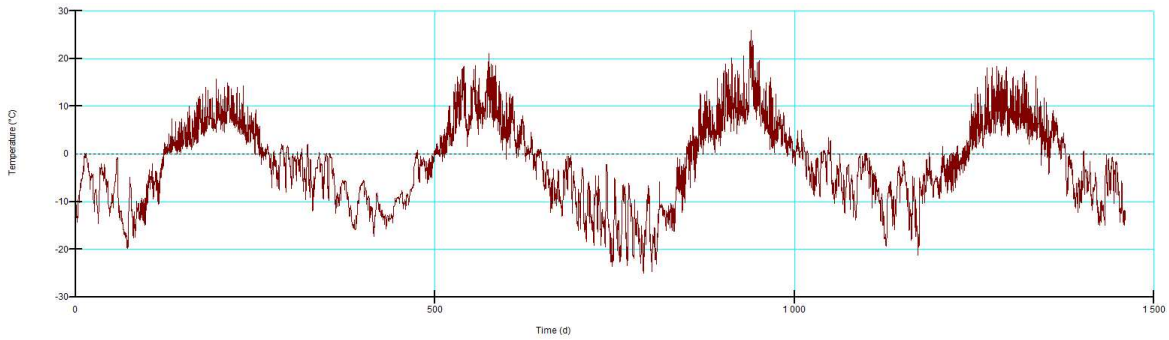

Figure 5.5 Ground surface temperature recorded in the borehole in UNIS-EAST side from January 1, 2018 until December 31, 2021, and applied as boundary conditions to run the first simulation to calibrate the model in Temp/W.

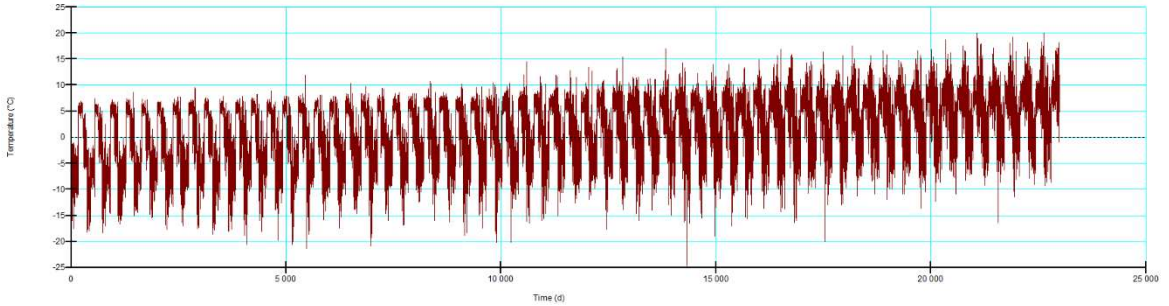

Figure 5.6 Temperature projections from SINTEF, applied as boundary condition at the ground surface when running the second simulation in order to obtain ground temperature profiles for the coming 61 years.

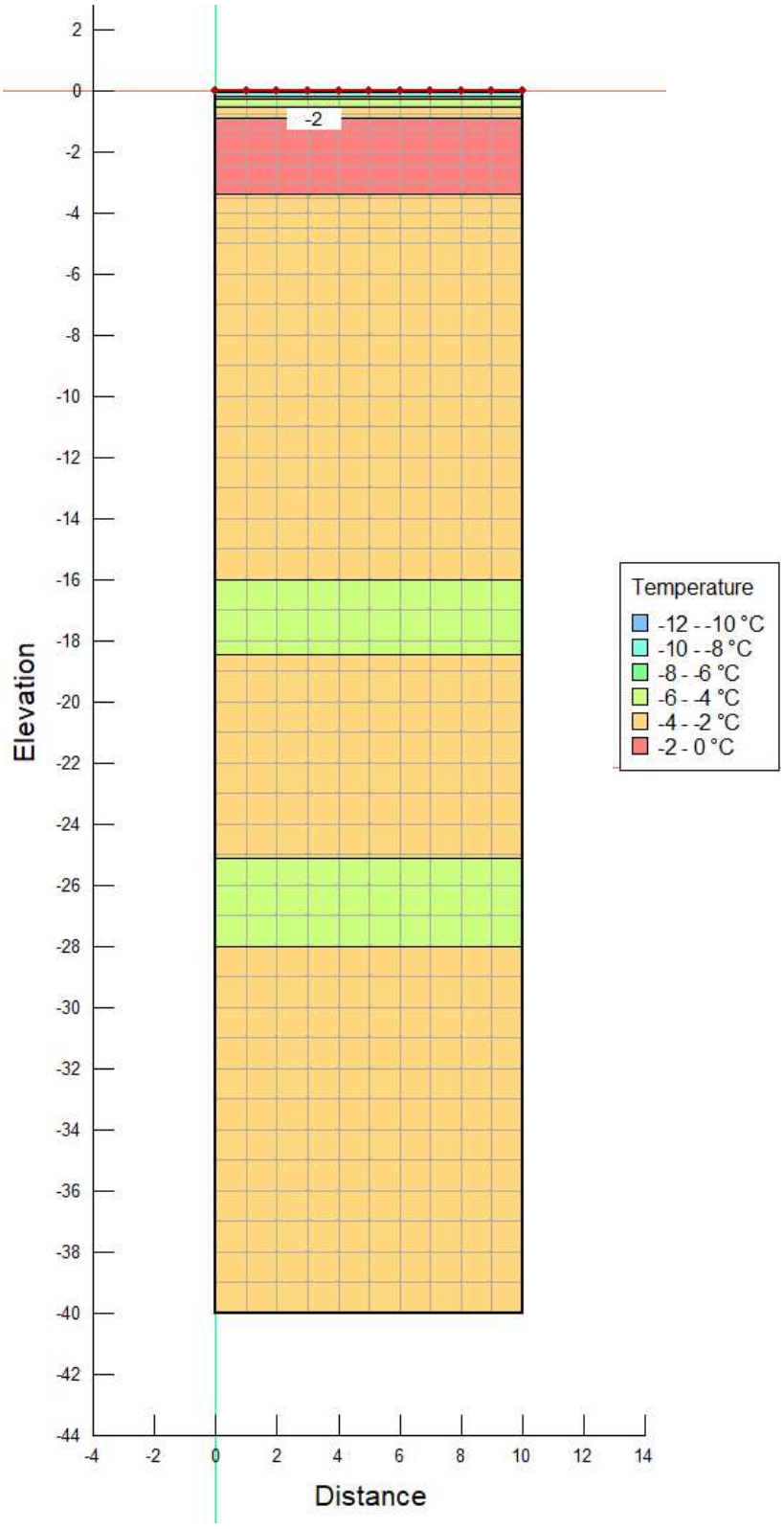

Figure 5.7 Initial temperature distribution for the thermal analysis. The x-axis represents he width of the considered soil region and the y-axis represents the ground depth from ground surface (0,00 m) to -40,00 m. The temperature distribution goes from -11,25°C at the top, to

-3,87°C at the bottom, marked with colors as shown in the figure, adapted (Kristin Enevoldsen, 2022).

Following the calibration of the model, measured ground surface temperatures spanning from 2018 to 2021 as an upper boundary condition are introduced. This initiates a simulation that runs for four years, with a timestep of 1 day. Subsequently, we create an interconnected derivative model, linked to the original. Within this framework, new boundary conditions are established. These updated parameters encompass the integration of predicted air temperatures for the extended period between 2022 and 2080 at the ground surface. The simulation is then conducted over a 62-year duration, employing daily time increments.

5.2.2 Geotechnical analysis

As outlined in Chapter 4, Section 4.3, the geotechnical analysis consists in two parts. After the collection of field data, the following step involved the computation of the volume and load characteristics associated with the three structures under investigation.
The results of these calculations are presented in Table 4.7 for reference and analysis.

	Big structure	Medium structure	Small structure
B (m)	0,225	0,18	0,15
L (m)	9,6	7,6	5,9
D (m)	2	2	2
A_b (m^2)	2,16	1,36	0,89
V (m^3)	36	19	6
Weight (kg)	17640	9310	2940
Load (N) (kN)	172,87	91,23	28,81
P (kPa)	80,03	66,69	32,01

Table 5.7 Cableway post structures' dimensions, volumes, and loads.

5.2.2.1 Bearing capacity analysis

According to the method presented in chapter 2, sections 2.6.2 and 2.6.3, the bearing capacity analysis has been carried out. Correction factors, which are displayed in the table below, are considered in the calculation.

Calculation method	Long-term actions	Variable actions	Ground properties (c)	Safety factor
Allowable stress	1,00	1,00	1,00	3,00

Table 5.8 Correction factors. s_c, d_c, i_c, b_c, and g_c are not considered, therefore they are placed equal to 1.

The following table shows the analysis results:

	Big structure	Medium structure	Small structurer
q_{ult} $[kN/m^2]$	223,88	224,97	225,75
P $[kN/m^2]$	80,03	66,69	32,01
q_a $[kN/m^2]$	74,63	74,99	75,25

Table 5.9 bearing capacity, maximum acting pressure, and allowable soil pressure.

$$P = \frac{N}{BL}$$

(5.1)

P is the maximum acting pressure, where N is the vertical load, B and L the width and length of the foundation base.

$$q_a = \frac{q_{ult}}{F_s}$$

(5.2)

A safety assessment of the bearing capacity must be conduct, ensuring that the applied pressure P does not exceed the allowable soil pressure q_a.

- Big structure: $q_a = 74{,}63 < P = 80{,}03$
- Medium structure: $q_a = 74{,}99 \geq P = 66{,}69$
- Small structure: $q_a = 75{,}25 \geq P = 32{,}01$

According to the model employed for estimating the ultimate bearing capacity, it is evident that the criteria for meeting ultimate capacity conditions are not satisfied. This situation raises concerns about the potential substantial settlement of large and medium-sized structures' foundations. It is important to note that not all structures will experience the same level of settlement, as variations in soil properties, temperature fluctuations, and external factors, such as meltwater streams in valleys and the occurrence of landslides, may exert varying degrees of influence in different areas.

5.2.2.2 Settlement analysis

To conduct a comprehensive settlement analysis, it is essential to calculate all three integral components of settlement assessment. This holistic approach ensures a thorough understanding of the structural response to various factors influencing settlement. The subsequent tables provide a comprehensive listing of values resulting from rigorous analytical calculations for each of these pivotal components, shedding light on the interplay between the elastic component, settlement due to ice melting beneath the foundation, and the creep settlement.

Circular footings	Strip footings	Rectangular footings		
0,125	0,262	Big str.	Medium str.	Small str.
		0,25859	0,25854	0,25836

Table 5.10 Influence factors calculated with (3.20), (3.21) and (3.21).

Elastic settlement (m)		
Big structure	Medium structure	Small structure
$68{,}1 \cdot 10^{-5}$	$45{,}6 \cdot 10^{-5}$	$18{,}2 \cdot 10^{-5}$

Table 5.11 Elastic settlement of the three structures of the cableway post using Equation (3.15), with the elastic module (E) set to 6000 and the Poisson's ratio (υ) set to 0,35.

"Melting" settlment (m)		
30 years	Δh_{2022_2052}	-0,0235
58 years	Δh_{2022_2080}	-0,0578

Table 5.12 Settlement due to melting ice in the ground below the foundation for the three structures of the cableway post in a timeframe of 30 and 58 years.

The soil porosity n has been calculated with Equation (3.17), resulting equal to 0,39 (39%), with dry density of soil ρ_{dry} equal to 1600 kg/m^3 and solid density ρ_{solid} equal to 2650 kg/m^3; the values of thawing depth $X(t)_{unfrozen}$ to calculate Δh_{2022}, Δh_{2052}, and Δh_{2080} are taken from .

Frozen soil type	b	n	w	σ_{c0} [kPa]
Ice-rich silt	1.00	3.00	0.60	71

Table 5.13 Creep parameters from Table 3.5

ρ_{wood} (kg/m^3)	490
θ_c (°C)	1
θ (°C)	2,1
$\sigma_{c\theta}$ (kPa)	139,98
$\dot{\varepsilon}_c$ (h^{-1})	0,0001
ε_f	0,1

Table 5.14 Variables Employed in the Calculation of Creep Settlement. θ denotes the average absolute temperature for the year 2016, measured at a depth of -2.00 meters below the ground surface, corresponding to the foundation depth.

	Creep settlement (m)		
	Big structure	Medium structure	Small structure
30 years	0,143	0,067	0,006
58 years	0,276	0,129	0,012

Table 5.15 Creep settlement for the three structures of the cableway post in a timeframe of 30 and 58 years. These values have been calculated by using Equation (3.18).

	Total settlement (m)		
	Big structure	Medium structure	Small structure
30 years	0,1664	0,0912	0,0298
58 years	0,3348	0,1881	0,0698

Table 5.16 Total settlement for the three structures of the cableway post in a timeframe of 30 and 58 years. They are the sum of the values listed in Table 5.11, Table 5.12 and Table 5.15; the elastic component, the settlement due to melting of ice beneath the foundation, and the creep settlement, rispectively.

Year	I_thawing (°C*days)	I_st (°C*days)	I_st (°C*sec)	X_t_unfrozen (m)	ALT comparison with 2022
2016	584,57	1169,15	101014214	1,56	
2017	589,32	1178,63	101833632	1,56	
2018	549,72	1099,43	94991098	1,51	
2019	601,62	1203,23	103959072	1,58	
2020	601,78	1203,56	103987757	1,58	
2021	630,69	1261,38	108983232	1,62	
2022	627,08	1254,17	108360115	1,61	
2023	611,52	1223,04	105671002	1,59	
2024	660,38	1320,75	114112973	1,65	0,04
2025	710,77	1421,53	122820192	1,72	0,10
2026	657,86	1315,72	113678381	1,65	0,04
2027	649,78	1299,57	112282502	1,64	0,03
2028	690,57	1381,14	119330842	1,69	0,08
2029	765,20	1530,40	132226560	1,78	0,17
2030	730,99	1461,97	126314381	1,74	0,13
2031	714,64	1429,28	123489619	1,72	0,11
2032	764,32	1528,64	132074323	1,78	0,17
2033	731,73	1463,45	126442253	1,74	0,13
2034	738,63	1477,26	127635091	1,75	0,14
2035	774,40	1548,81	133817011	1,79	0,18
2036	848,82	1697,65	146676787	1,88	0,26
2037	860,42	1720,83	148680058	1,89	0,28
2038	863,06	1726,11	149136077	1,89	0,28
2039	854,50	1709,00	147657773	1,88	0,27
2040	954,56	1909,12	164948141	1,99	0,38
2041	948,44	1896,89	163890950	1,98	0,37
2042	886,01	1772,01	153101664	1,92	0,30
2043	917,73	1835,47	158584435	1,95	0,34
2044	936,78	1873,55	161875066	1,97	0,36
2045	982,33	1964,66	169746797	2,02	0,41
2046	1028,23	2056,47	177678835	2,06	0,45
2047	1056,95	2113,89	182640096	2,09	0,48
2048	1054,02	2108,04	182134656	2,09	0,48
2049	1052,63	2105,25	181893773	2,09	0,48
2050	1154,18	2308,35	199441440	2,19	0,57
2051	1176,29	2352,59	203263430	2,21	0,60
2052	1175,48	2350,96	203123290	2,21	0,59
2053	1268,20	2536,39	219144269	2,29	0,68
2054	1176,84	2353,67	203357261	2,21	0,60
2055	1282,93	2565,87	221690995	2,31	0,69
2056	1270,85	2541,69	219602189	2,29	0,68
2057	1293,20	2586,40	223464960	2,31	0,70
2058	1236,50	2473,01	213667891	2,26	0,65

2059	1322,66	2645,32	228555821	2,34	0,73
2060	1320,19	2640,37	228128314	2,34	0,73
2061	1444,25	2888,50	249566054	2,45	0,83
2062	1461,63	2923,27	252570355	2,46	0,85
2063	1555,52	3111,04	268794202	2,54	0,93
2064	1499,40	2998,80	259096493	2,49	0,88
2065	1563,06	3126,12	270096941	2,54	0,93
2066	1614,00	3228,01	278899891	2,59	0,97
2067	1637,90	3275,81	283029811	2,60	0,99
2068	1666,59	3333,18	287986579	2,63	1,02
2069	1739,78	3479,55	300633293	2,68	1,07
2070	1786,84	3573,68	308766125	2,72	1,11
2071	1786,00	3572,00	308620800	2,72	1,11
2072	1826,96	3653,92	315699034	2,75	1,14
2073	1885,91	3771,82	325885075	2,80	1,18
2074	1875,31	3750,61	324053050	2,79	1,18
2075	1942,82	3885,64	335719296	2,84	1,23
2076	1954,19	3908,37	337683341	2,85	1,23
2077	1987,39	3974,77	343420474	2,87	1,26
2078	2117,76	4235,51	365948064	2,96	1,35
2079	2119,56	4239,12	366259968	2,96	1,35
2080	2277,47	4554,94	393546816	3,07	1,46

Table 5.17 Forecasted thawing depths from SINTEF data. The table displays thawing indexes spanning the years 2016 to 2080, along with their corresponding ALT values. The last column presents ALT comparisons between the current year, 2022, and the subsequent years up to 2080.

6 Discussion

In light of the aims of the study, presented in Chapter 2, the upcoming chapter will conduct comparative analyses across multiple methodologies employed to assess active layer thickness, temperature projections within the soil, and their impact on active layers, soil bearing capacity, and foundation settlement attributed to the increase of temperatures.

The constraints inherent to these methodologies, arising from the inherent limitations of the models themselves, presented in Chapter 7, and the absence of in-situ data, will be brought to the forefront. As a result, the selection of generic data extracted from the existing literature for the frozen soil under investigation becomes a rational choice.

The examination of these methodologies aims to highlight the steps, data utilization, and overarching findings of the comprehensive study.

At first, the results from the analytical models are presented; then those modeled with the Temp/W software, and both will be compared with the real data measured in the borehole. It will become immediately evident that the temperature curves produced by the analytical model proposed by Orlando B. Andersland, 2003, exhibit notable discrepancies, while a distinct convergence is observed in relation to those obtained through the numerical model. The figures presented in Figure 6.? also serve to illustrate the effective calibration of the Temp/W model. This successful calibration sets the stage for the subsequent phase of our study, wherein forecasted air temperatures are integrated into the software to compute soil temperatures. Subsequently, the resulting dataset is exported to an Excel spreadsheet, and temperature profiles for the years 2052 and 2080 are plotted.

Another approach for forecasting the thickness of the active layer in the future involves the application of Stephen's formula. By utilizing projected temperature data, this method enables the estimation of active layer deepening over the course of the next 62 years.

Following, the calculation of the bearing capacity and the analysis of foundation settlements are discussed. These aspects are intricately linked to temperature fluctuations, particularly given that the foundations of the examined structures are shallow, situated approximately 2.00 meters below the ground surface. Therefore, the thawing and refreezing of the soil has a great impact on them.

6.1 Comparison between the analytical solution and real soil temperature profiles

The results from the analytical solution indicate an overestimation of both the Active Layer Thickness (ALT) and permafrost temperatures when compared to field measurements. Specifically, the field measurements reveal a thinner active layer than what is predicted by the analytical solution. For instance, at the peak thawing period in September 2020, the analytical solution predicts an active layer depth of 3,00 meters, whereas the observed data indicate an active layer depth of only 1,00 meters.

Furthermore, when examining ground temperatures at a depth of 15,00 meters during the same period, Figure 6.2 demonstrates that the analytical solution yields a temperature of approximately -2,00 °C, whereas the observed data records a lower temperature of -4,00°C, during the month of Septemebr, when the thickest active layer has been recorded.

This discrepancy can be partly explained by the different air temperatures of the sites and variations in the soil properties. The analytical calculations were conducted using general soil property values from Orlando B. Andersland, 2003. The analytical calculations were conducted using general soil property values.

If the foundation design had relied solely on the analytical solution, it would have introduced a considerable margin of safety well above the actual environmental conditions. This is primarily attributable to the fact that the design would have been formulated assuming a warmer permafrost and a thicker active layer than what exists in reality. In essence, the calculated design parameters would have been conservative, ensuring a significant safety buffer against potential ground-related challenges.

In practice, this cautious approach may be viewed as an excessively safe and potentially uneconomical solution. The rationale behind this is that, in the actual field scenario, the active layer is notably thinner, and the permafrost temperatures are colder. As demonstrated by the recorded temperature of -4.00°C, in stark contrast to the -2.00°C calculated using the analytical solution at a depth of 15,00 meters.

Consequently, while the foundation design derived from the analytical solution would undeniably provide a high level of safety and resilience against environmental uncertainties, it might not align with economic efficiency principles. Achieving a balance between safety and cost-effectiveness is a paramount consideration in engineering and construction. It underscores the importance of adopting a more nuanced and site-specific approach to

foundation design in permafrost regions, taking into account both safety requirements and economic viability.

As outlined in the methodology chapter, Section 4.1, the foundation design process necessitates consideration of climate variations. This involves conducting design analyses for the warmest three years within the most recent three decades. By adhering to this approach, the analysis was intended to encompass the years 2016, 2020, and 2022, utilizing the various methods introduced earlier in this study. Unfortunately, the availability of observed data presented a challenge, as data for the years 2016 and 2022 were unavailable. In view of this constraint, the analysis could only be performed for the year 2020, where observed data were accessible. The unavailability of data for 2016 and 2022 underscores the importance of data continuity and highlights a limitation in the study's ability to examine the warmest years within the specified timeframe. This limitation underscores the importance of acknowledging data constraints and adaptively addressing them in the context of foundation design in climate-variable environments.

6.1.1 Orlando B. and Andersland method limitations

In the realm of geotechnical engineering, the analysis of subsurface temperature variations is instrumental in understanding ground behavior. For the visualization of these temperature fluctuations over time and depth Trumpet curves are often used. However, a noteworthy limitation emerged during the course of this study when examining Trumpet curves for the years 2016, 2020, and 2022. It has been observed that temperature differences at depths greater than 6 meters displayed unexpectedly significant shifts.

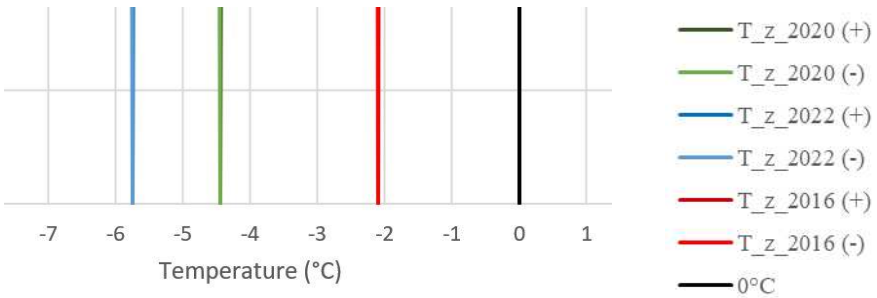

Figure 6.1 Temperatures in the ground at 20,00 meters depth

In fact, as can be seen in Figure 6.1 Temperatures in the ground at 20,00 meters depth, the temperature in the ground at -20 meters for 2016, 2020, and 2022 is respectively -2,05°C, -4,45°C and, -5,75°C. These pronounced temperature variations in the lower layers for closely spaced years contradict the conventional understanding that subsurface temperatures tend to exhibit greater stability with increasing depth.

In light of this finding, it becomes crucial to question the accuracy and reliability of the modelling methodologies employed. The suggested method is, in fact, reliable for modelling the temperature fluctuations in the uppermost layers and for visualizing the temperature tendency with the soil beneath a depth of 6 meters. It can be asserted that this method is qualitatively sound, as it correctly represents temperature trends; however, it may not be quantitatively accurate.

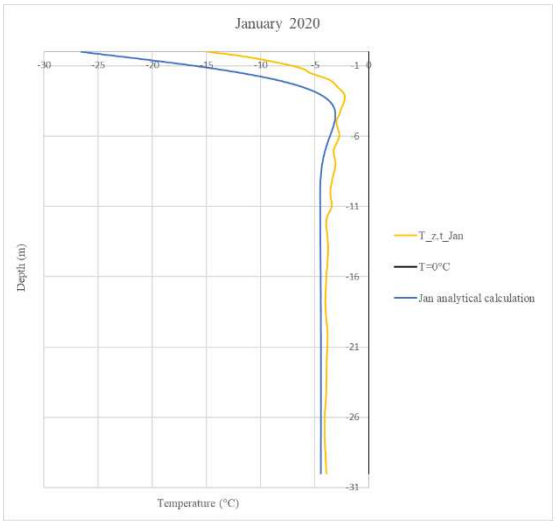
January 2020
Depth (m)
Temperature (°C)
T_z,t_Jan
T=0°C
Jan analytical calculation

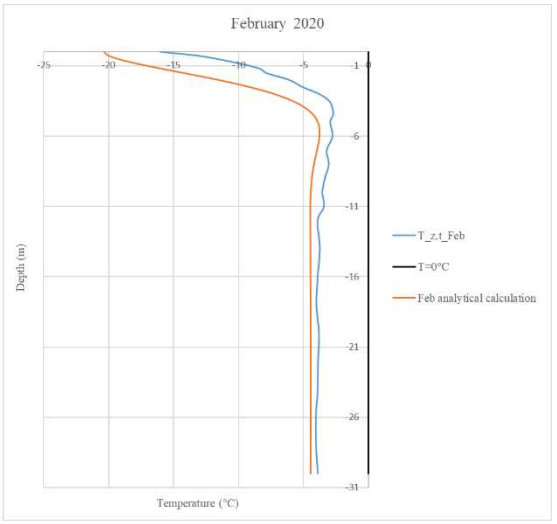
February 2020
Depth (m)
Temperature (°C)
T_z,t_Feb
T=0°C
Feb analytical calculation

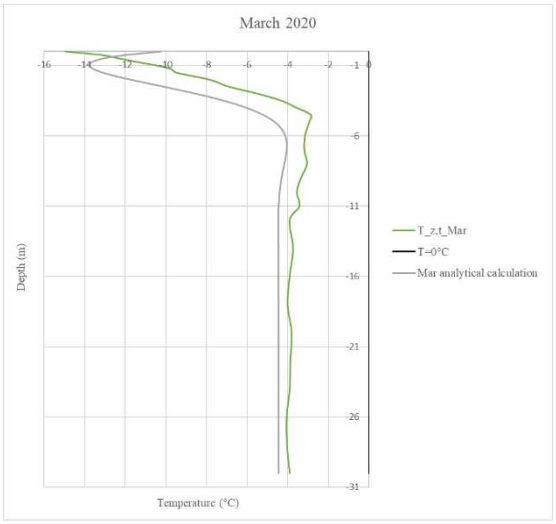
March 2020
Depth (m)
Temperature (°C)
T_z,t_Mar
T=0°C
Mar analytical calculation

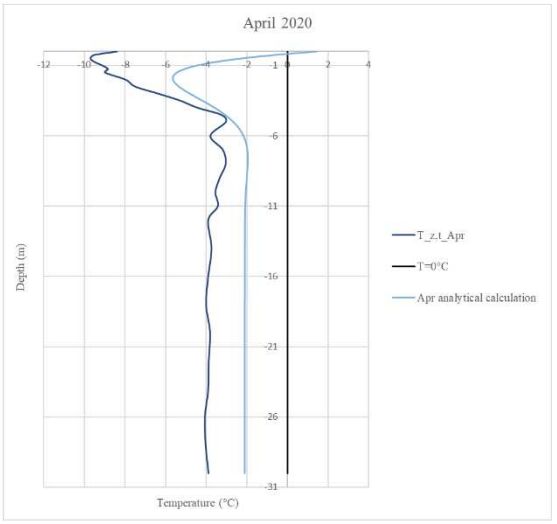
April 2020
Depth (m)
Temperature (°C)
T_z,t_Apr
T=0°C
Apr analytical calculation

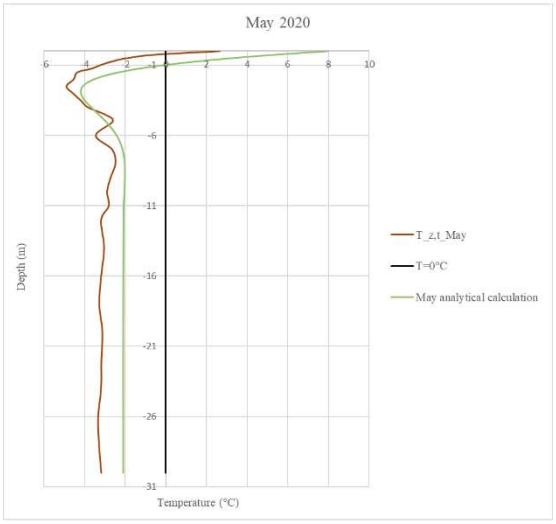
May 2020
Depth (m)
Temperature (°C)
T_z,t_May
T=0°C
May analytical calculation

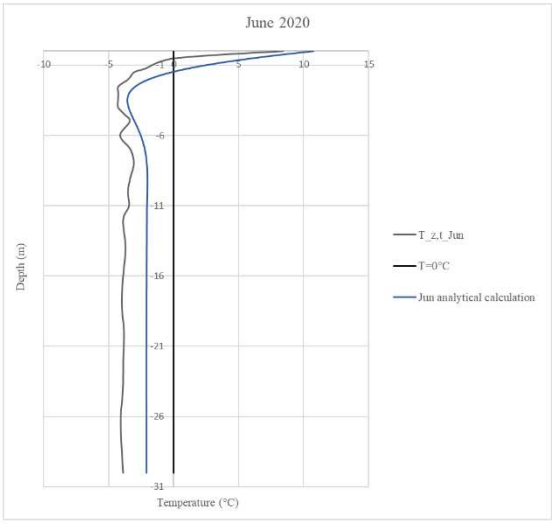
June 2020
Depth (m)
Temperature (°C)
T_z,t_Jun
T=0°C
Jun analytical calculation

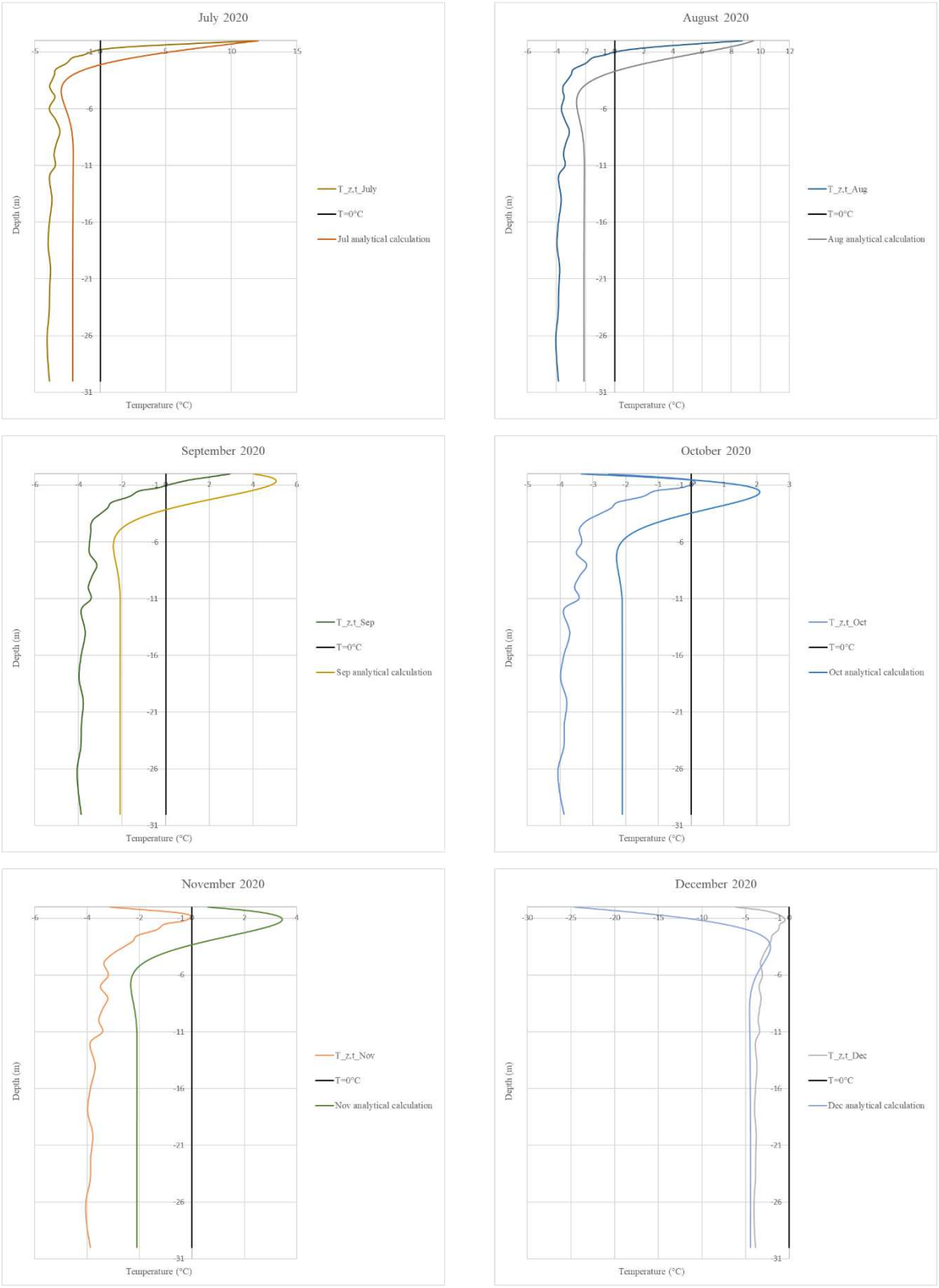

Figure 6.2 Comparison of ground temperature profiles calculated utilizing the numerical method by Orlando B. Andersland, 2003, and ground temperature profiles recorded by the thermistor strings.

6.2 Temp/W transient analysis

A transient analysis is run to warm the ground and introduce seasonal fluctuations. The analysis is started on 01 January 2018 and runs for 4 years (31 Decemebr 2021), saving the temperature profile every day, adapt from (Heller, 2021). The outputs for this first simulation are showed in Figure 6.2.

As evident from the graphs in Figure 6.3, the dataset within the model generated using Temp/W exhibits a high level of reality fidelity. The temperature profiles within the soil, as derived from observed data, closely align with the temperature profiles calculated by the software. It's noteworthy that the sole exception to this concordance is the month of May, which had previously demonstrated a misfit when plotting temperature curves based on thermistor-string measurements. This discrepancy is likely attributed to a system malfunction during that particular month. However, the overall favorable alignment between observed and calculated temperature profiles serves as an indication that the model is well-calibrated. This ensures that the model is ready to accommodate new input data, facilitating the continuation of the study.

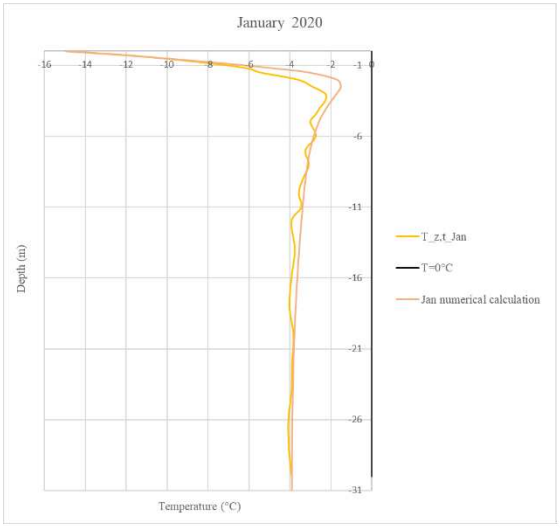
January 2020
Depth (m)
Temperature (°C)
T_z,t_Jan
T=0°C
Jan numerical calculation

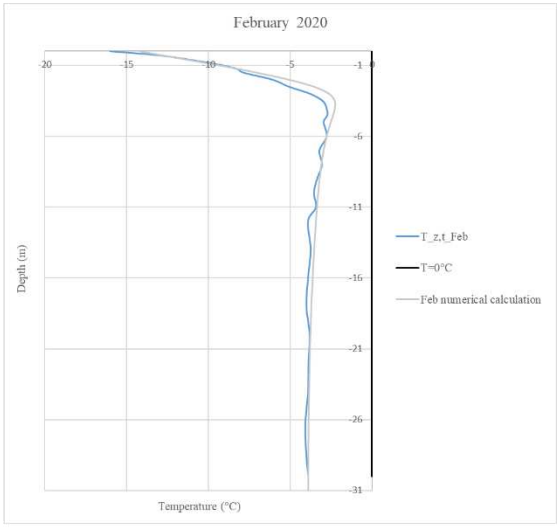
February 2020
Depth (m)
Temperature (°C)
T_z,t_Feb
T=0°C
Feb numerical calculation

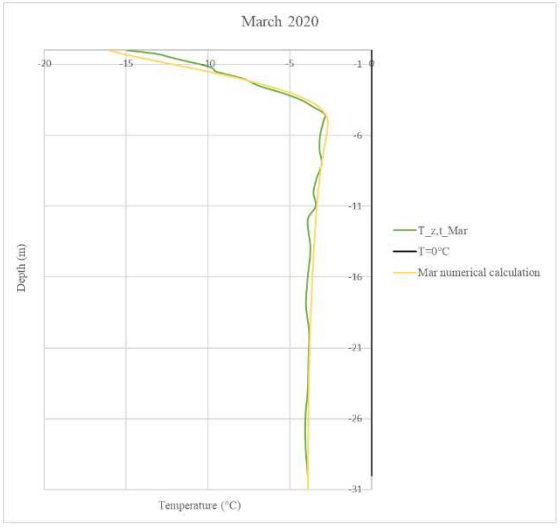
March 2020
Depth (m)
Temperature (°C)
T_z,t_Mar
T=0°C
Mar numerical calculation

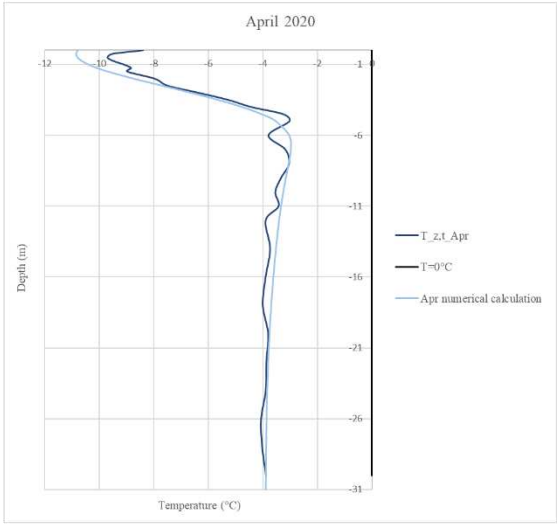
April 2020
Depth (m)
Temperature (°C)
T_z,t_Apr
T=0°C
Apr numerical calculation

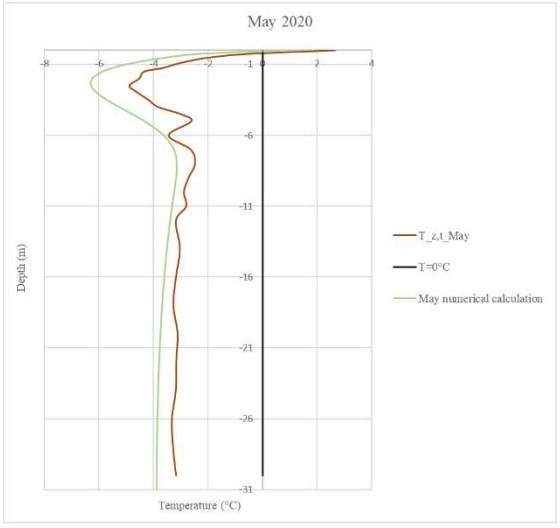
May 2020
Depth (m)
Temperature (°C)
T_z,t_May
T=0°C
May numerical calculation

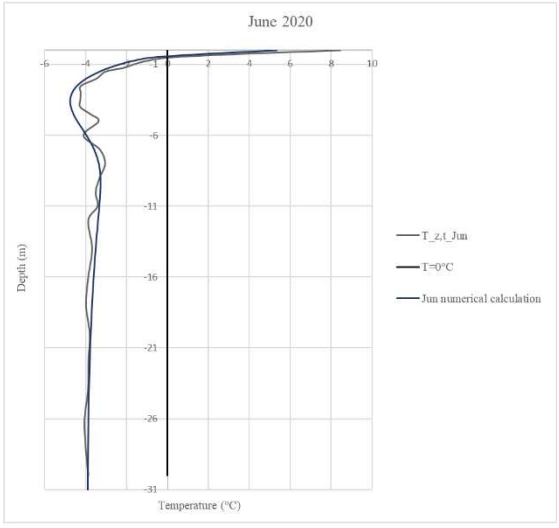
June 2020
Depth (m)
Temperature (°C)
T_z,t_Jun
T=0°C
Jun numerical calculation

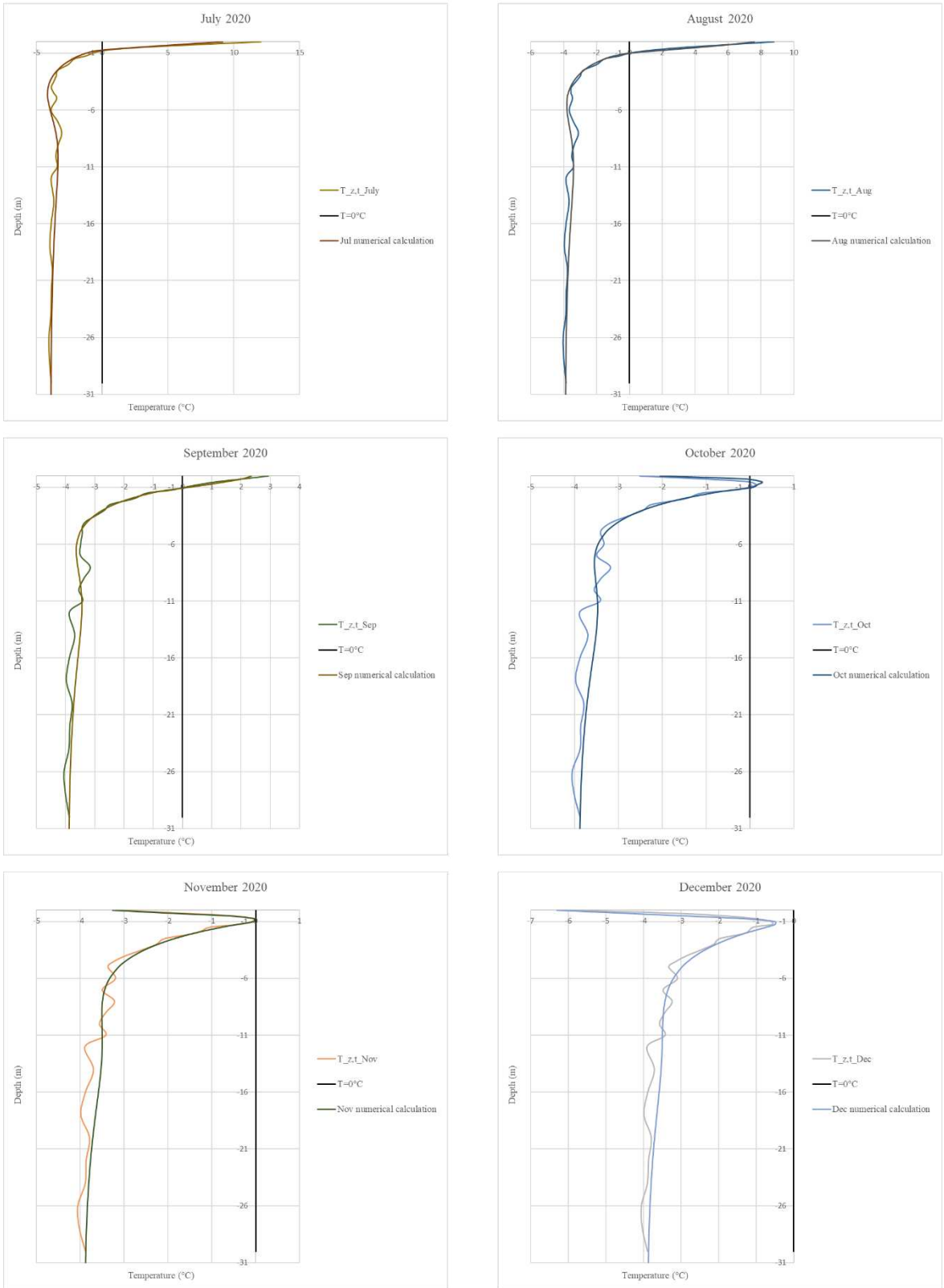

Figure 6.3 Comparison of modelled temperature profiles resulting from Temp/W calibration process and measured temperature profile from thermistor-strings placed at UNIS-EAST borehole.

6.2.1 Forecasted ground temperature fluctuations

Based on the Temp/W model simulations of ground temperatures, two graphs have been plotted. The first graph, displayed in Figure 6.4, illustrates the ground temperature profile for the entire 2052. Meanwhile, Figure 6.5 presents the ground temperature profile for the year 2080. For the year 2052 is noticeable that the month with the thickest active layer is December with a thaw penetration of 1,50 meters; while for year 2080 the month that presents the greatest ALT is May, with the ice front reaching a depth of 7,00 meters.

Comparing the two graphs reveals substantial disparities in temperature profiles. Specifically, in the case of the year 2052, temperature fluctuations are predominantly concentrated between depths of 2,00 to 2,50 meters below the surface. However, in the context of the year 2080, a notable shift is evident, with the temperature profile shifting considerably to the right (where positive temperatures are encountered). This shift is accompanied by pronounced temperature variations extending as deep as 6,00 meters.

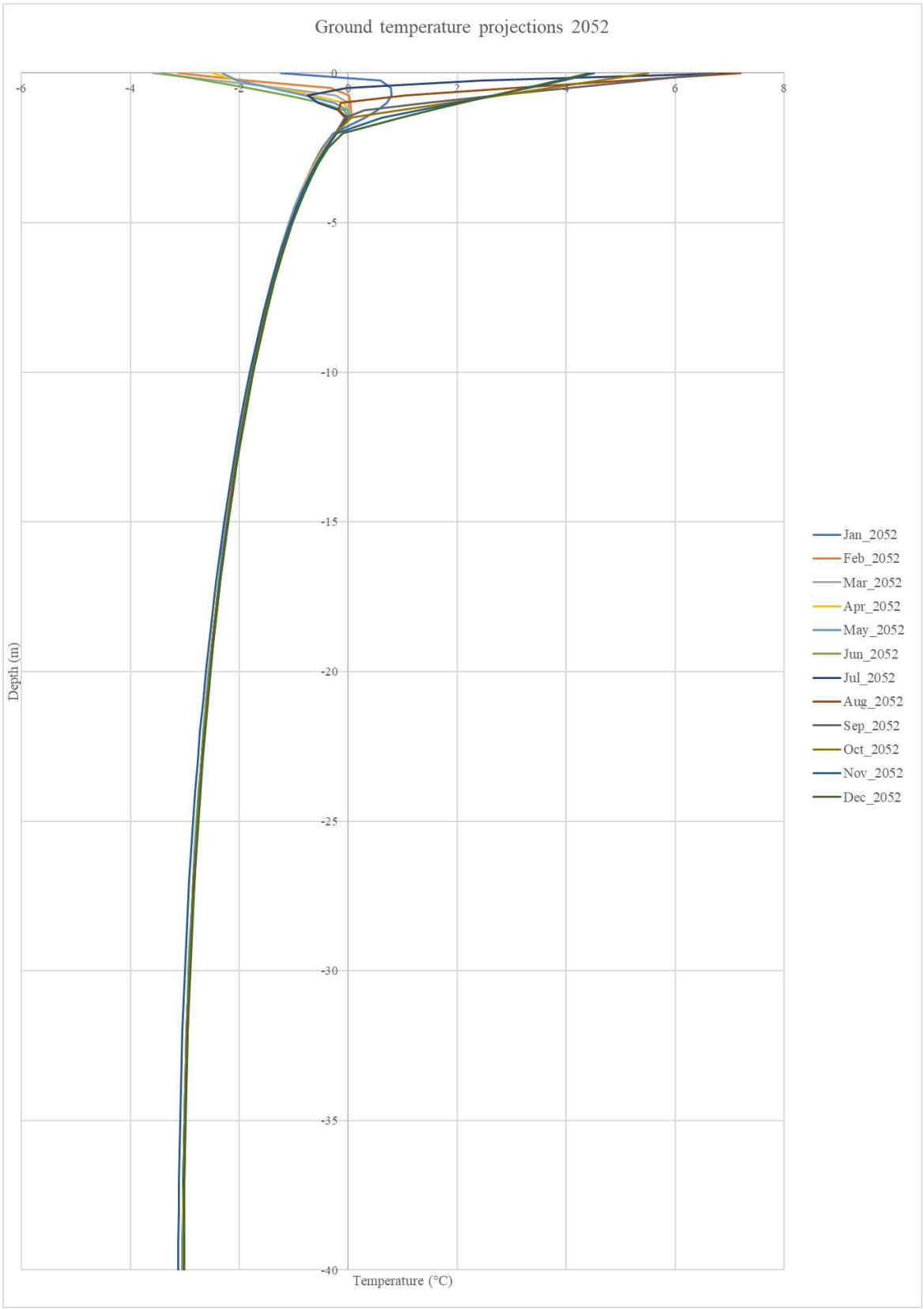

Figure 6.4 Ground temperature profile for the year 2052

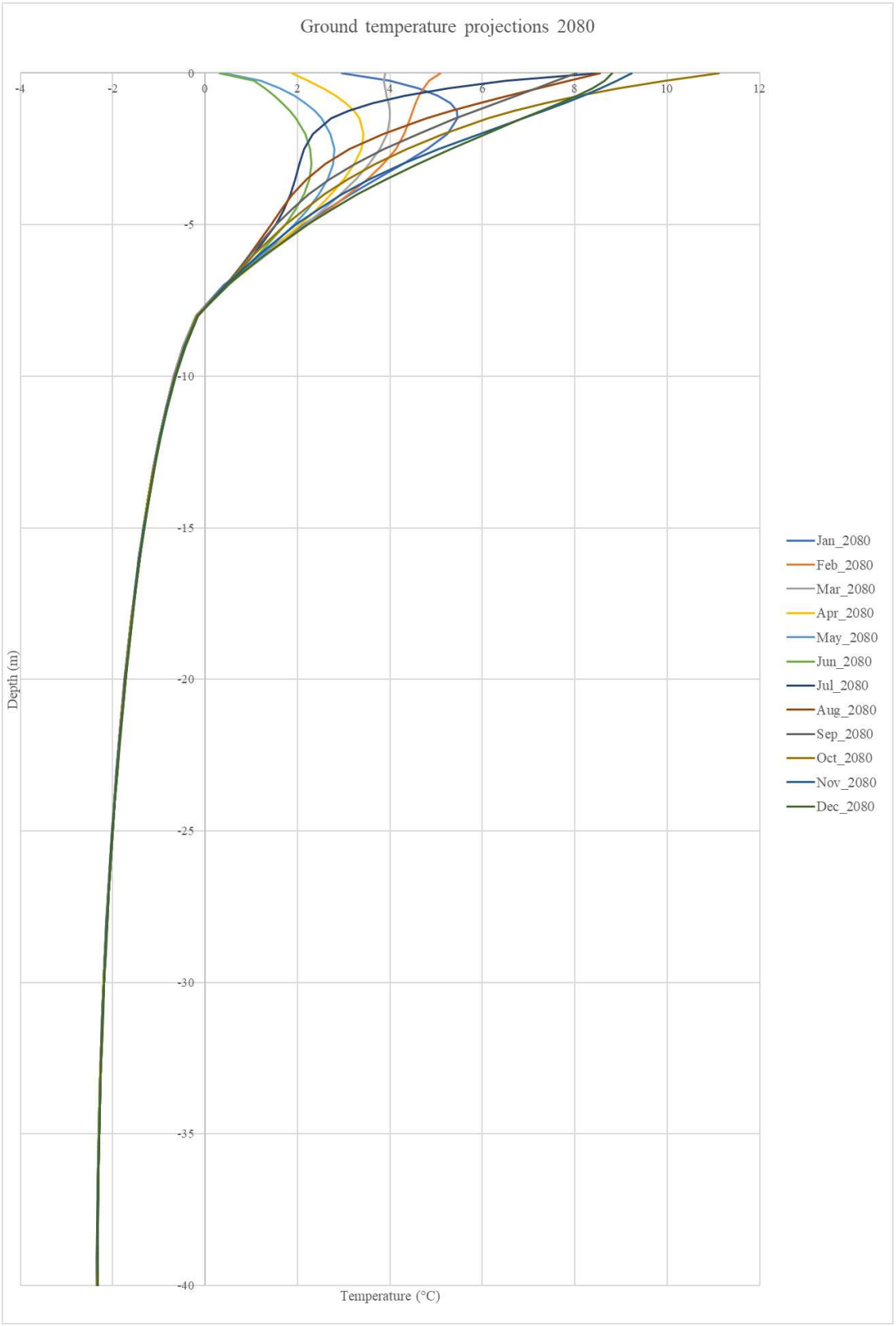

Figure 6.5 Ground teperature profile for the year 2080

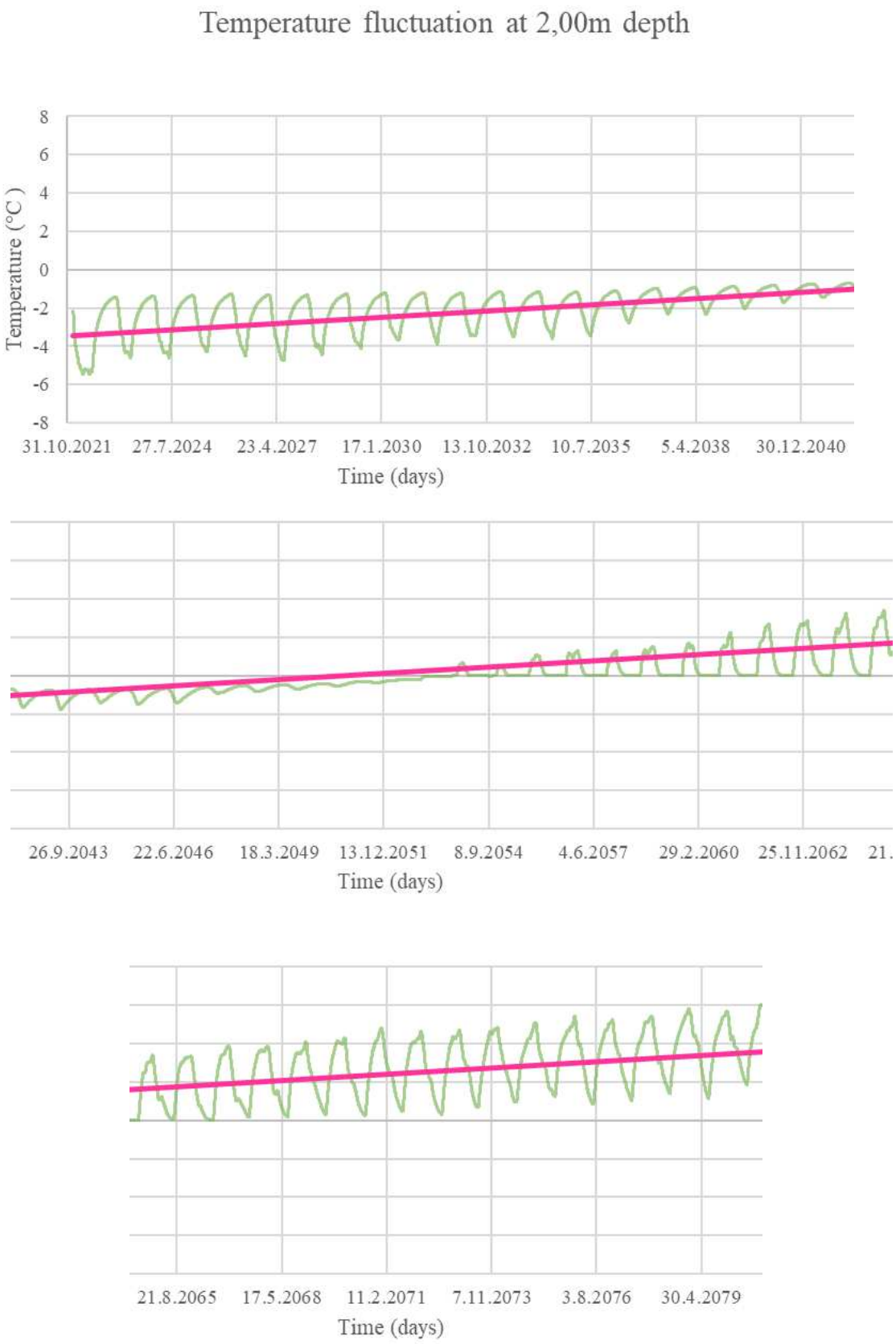

Figure 6.6 Temperature fluctuation at 2,00 meters depth from 2021-2080.

From the data exported from the simulation run with Temp/W the graph in Figure 6.6 has been plotted. It shows the temperatures at foundation depth from 2021-2080. A notable observation within this data set is that, starting from 2053, precisely October 2053, he subsurface soil at a depth of 2.00 meters consistently maintains positive temperatures. starting from November 2045, temperatures no longer plummet below the critical -1°C threshold, thus ensuring that the soil remains unfrozen throughout the ensuing decades, a critical insight for various engineering and environmental considerations.

6.3 Stephan's equation method

Stephan's equation has been employed to project the active layer thickness using data forecasted by SINTEF. This data visualization will serve as a valuable tool for future research, enabling the comparison of foundation depths and active layer thicknesses. Through this comparison, it is possible to determinate when the active layer will surpass the foundation depth.

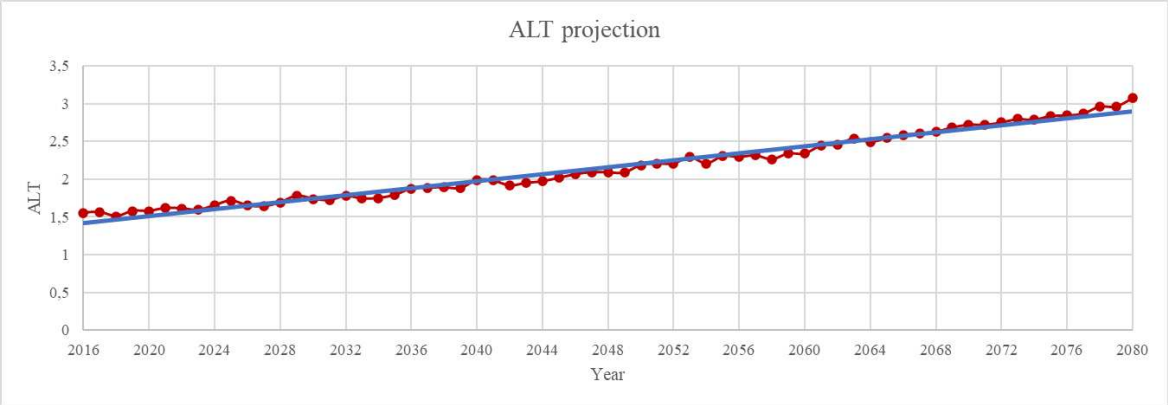

Figure 6.7 ALT projection curve and its linear approximation, from year 2016 until 2080.

Unfortunately, there is no knowledge of the real depth of the foundation for all the structures of the post cableway. Out of approximately 230 structures, only a fraction has undergone renovation. When it is decided that a structure must be refurbished, a specific management of it is carried out and a careful study of the foundations is performed.

While some insights into foundation depths can be retrieved from the Store Norsk archives, it is evident that when the decision to restructure a specific structure is made, the integration of digital tools becomes essential for conducting a more precise analysis. This digital approach enables a broader comprehension of the system and facilitates informed decision-making on how to proceed.

When accurate measurements are made, it is then possible to compare the specific and actual foundation depths with the depth of the active layer.

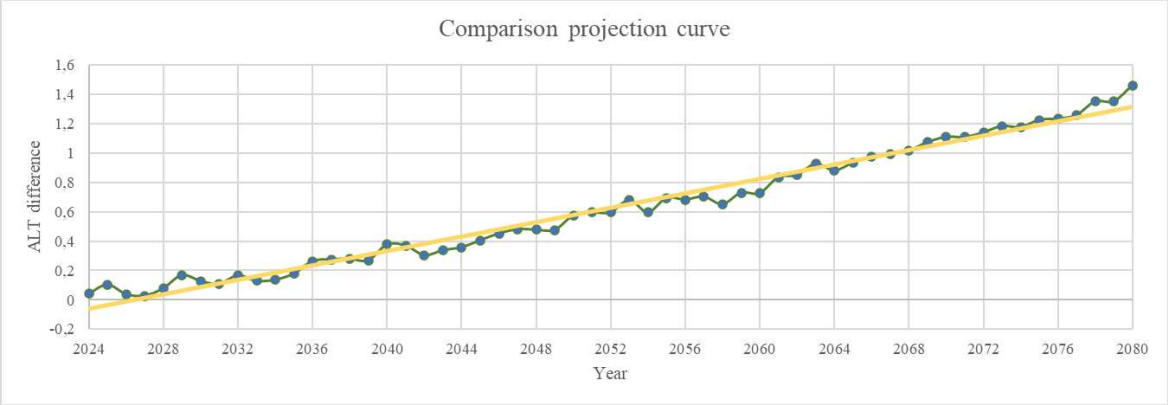

Figure 6.8 ALT comparison curve and its linear approximation, between year 2022 and the upcoming years from 2024 until 2080.

The graph presented in Figure 5.5 has been generated using data provided in Table 5.17. This visualization serves for observing the anticipaded variations in active layer thickness over the forthcoming decades. The interpolation line, highlighted in yellow, looks quite steep, extending from an approzimate 4 cm increase in 2024 up to 1,45 m by the year 2080.

6.3.1 Stephan's equation method limitations

Within the identified limitations stemming from the application of Stephan's equation, it is important to acknowledge that the selected n-factors are not specifically tailored for silty soil; instead, they were derived from data related to sand and gravel. This limitation arises from the unavailability of n-factors tailored to the chosen material. As a pragmatic approach, n-factors associated with the most analogous materials were utilized.

Another limitation of this study arises from the nature of the equation itself, which focuses on calculating the thickness of the active layer. This limitation becomes apparent in the inability to compare temperature trends, as the scope of the equation is to calculate the thickness of the active layer. Consequently, it does not provide a broader perspective on temperature variations within the context of the problem.

6.4 Bearing capacity and settlements analyses of shallow foundations

In the field of geotechnical engineering, the assessment of bearing capacity and settlements in frozen soils presents a set of challenges and complexities. The frozen subsurface, influenced by temperature variations and the interplay of various geophysical factors, demands a meticulous analysis to ensure the safety and stability of structures.

In this chapter an authentic solution for the assessment of bearing capacity and settlements in frozen soils is delved.

6.4.1 Bearing capacity analysis

Upon conducting a comprehensive assessment of the bearing capacity, it becomes evident that the representative structures categorized as "big" and "medium" fail to meet the safety criteria, while the "small" structures seemingly do. However, this initial assessment does not accurately reflect the true scenario on the field.

In reality, the "small" structures are not immune to the issue of settlement. During a field survey conducted in September in Adventdalen, it became apparent that some structures along line 5-6 exhibited noticeable settlement, resulting in increased inclinations compared to the winter conditions (see

Figure 6.9). This behavior challenges the previous assumption that "small" structures remained unaffected.

The observed settlements and increased inclinations are believed to be attributed, at least in part, to the presence of water in the subsoil. This observation underscores the dynamic nature of the subsurface conditions and the potential impact on structures of varying sizes.

Further examples of structures at risk can be found along the same line (5-6), particularly those situated in proximity to streams or areas prone to landslides (Figure 6.10). This highlights the multifaceted nature of the challenges faced by the structures in this region, where a combination of factors, including soil properties, hydrology, and geological phenomena, contribute to the observed settlement and tilting issues.

In light of these findings, it will be essential, in further studies, to reevaluate the assessment criteria and consider a more comprehensive approach that accounts for the dynamic nature of the subsoil and the potential risks posed to structures of all sizes. Addressing these

challenges effectively will be pivotal in ensuring the long-term stability and safety of the structures within the study area.

Figure 6.9 Small structure settlement and displacement

Figure 6.10 Rock and land-slide adjacent to the structure and stream flowing at the base of the structure.

6.4.2 Settlements analysis

The evaluation of structural performance, or structural health, hinges upon the comparison between allowable settlements and the actual settlement experienced by structures. For instance, in the context of residential buildings, Instans Arne, 2017, delineates criteria over a 30-year timeframe as follows:

- “Good” for settlements (s) ≤ 5 cm
- “Acceptable” for settlements between 5 cm < s < 10 cm
- “Failure” for settlements ≥ 10 cm

While these criteria are originally designed for residential buildings, they may prove overly stringent when applied to "industrial" structures. However, any specific structural analysis to derive alternative criteria has been performed. Consequently, the assessment will be based on the criteria established for residential buildings.

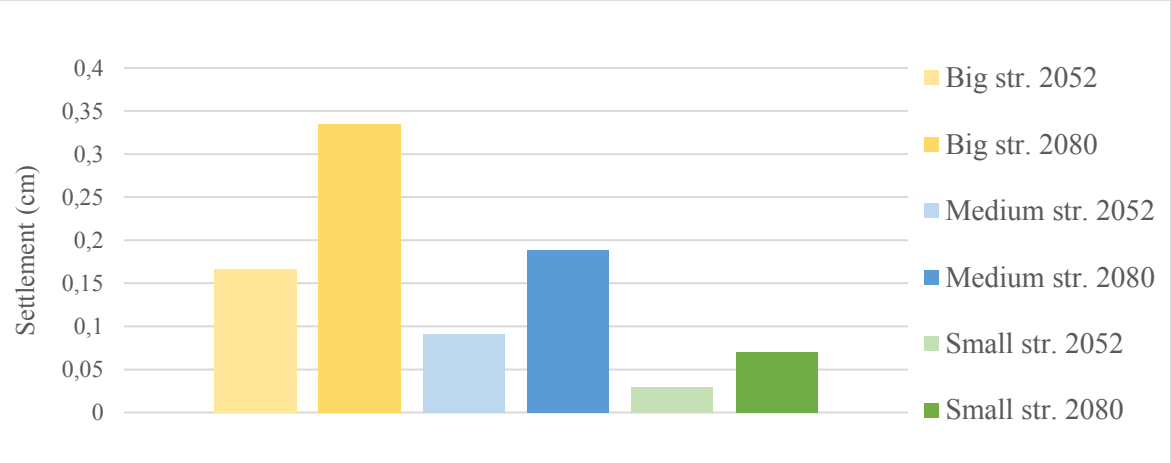

Figure 6.11 Cableway post structures’ settlement trends for the years 2052 and 2080.

As outlined in the methodology section, Instans Arne, 2017, provides criteria for assessing the performance of foundations in frozen soil. According to (Instans Arne, 2017, if the settlement over a 30-year period remains below 5 cm, it can be classified as “good”. Figure 6.11 and Table 5.17, illustrates that only the settlement of the smaller structure during the initial 30 years and between 2052 and 2080 meets this criterion, with a settlement of 2,90 cm in the first 30 years and an increment of 4,00 cm in the following 28 years.

Within the range of 5 cm to 10 cm, Instans Arne, 2017, considers the settlement as “acceptable”. Here the medium-sized structure, at the limit of this category, it experiences

30 years, a settlement of 9,10 cm over the first 30 years, followed by a 9,60 cm increase in the subsequent 28 years.
However, if settlement exceeds 10 cm, it falls into the "failure" category. Here, it is possible to observe such settlements for the big structure between 2022 and 2052 and between 2052 and 2080, with the settlement reaching nearly 17 cm.
This observation does not hold uniformly for all small structures, as the investigation field in Adventdalen have revealed. It has come to attention that a subset of these small cableway post is experiencing noticeable sinking (in some cases approximately half of a meter) and tilting. In fact, a significant number of these structures appear to be on the verge of structural failure. Refer to the accompanying photographic evidence for a visual representation of these concerning developments.

Previous calculations regarding the sub-surface ice melt beneath the foundation have exclusively considered the ice contained within the soil pores. This limitation is evident in the modest settlement outcomes presented in Table 5.12. To conduct a more precise analysis, it is necessary to incorporate the presence of ice lenses within the soil beneath the foundation. The thawing of these ice lenses has the potential to induce a significant decrease in the foundation level. For instance, if an ice lens, measuring 3 cm in thickness, were to melt, the foundation would experience an abrupt descent of 3 cm.

These findings underscore the complexity of the environmental factors and geotechnical conditions within Adventdalen. While some small structures remain stable, others are evidently vulnerable to significant deformation and potential collapse. This variability in structural behavior warrants further investigation and analysis within the broader context of this research. In this regard, data on surface and sub-surface temperatures from i-bottoms that had been deployed a year ago have recently been collected.

7 Conclusions

This research delved into the intricate relationship between climate change and the structural stability of Longyearbyen's historical heritage, focusing on the foundations of the cableway post structures. Climate change has led to a constant increase in air temperatures, thereby influencing the thermal conditions of the underlying soil. As external temperatures rise, the ground temperature experiences a significant increase, especially within the upper soil layers. The impact of air temperature decreases with increasing depth, revealing through direct observations and numerical modeling that temperatures remain relatively stable between depths of 25-30 meters and 40 meters over a span of more than six decades.

The foundations of the structures in question are shallow, rendering them highly susceptible to temperature fluctuations. To represent the different structural scales, sample structures representing three categories have been selected: large, medium, and small. The analyses detailed in Chapter 5 revealed that the foundations of larger and medium-sized structures are most vulnerable to failure and subsidence. However, during a field investigation, significant settlement issues affecting even the foundations of smaller structures have been observed.

This highlights the efficacy of the analytical model used for providing a preliminary understanding of the problem. Nevertheless, for more accurate results, it is necessary to conduct in-depth assessments tailored to each specific case. This entails studying the in-situ soil composition and accounting for additional external factors, such as landslides and the presence of streams and taliks.

An initial investigation into the impact of climate change on Arctic soil and its historical and cultural heritage has been conducted. In the discussion chapter, the presentation of graphs depicting the upward trend in the active layer serves as a foundational element for exploring the changing thermal dynamics of Arctic soil. These consistently ascending curves indicate an ongoing process of warming and subsequent ice melt within the soil, which is projected to persist in the coming years. This phenomenon is expected to have significant repercussions for the region's structures, particularly those of historical importance.

As part of this preliminary study, generic soil modeling parameters available in the existing literature were considered. The subsequent calculations were aimed at providing a preliminary glimpse into potential future scenarios and offering insight into the expected consequences of permafrost thaw on the existing structures.

7.1 Further work

Although not reported in the core of the thesis, a significant amount of time was dedicated to fieldwork. Numerous structures from the post-cableway era, including Taubanecentralen and Tarubanestasjonen, underwent investigation utilizing a dGPS (differential GPS) technology. This was done in order to record data relating to the elevation of the base of the structures that rely on the pillars of the foundation. The intention is to repeat these accurate measurements in the future and then compare the previously recorded data with outcomes derived from analytical and numerical models. This calibration process will enable us to generate fresh predictions regarding settlements.

The overarching goal of both the completed and forthcoming studies is the preservation of the Arctic's historical heritage to the greatest extent possible. Therefore, it is advisable to conduct more comprehensive and structure-specific investigations, focusing on those structures that appear to be most vulnerable. Site investigations and lab tests to get in situ soil parameters are therefore recommended.

While some structures have already been renovated, many others are awaiting restoration. Furthermore, this task is not straightforward, the aim is to maintain the integrity of the original structures, even in cases involving subterranean interventions. This endeavor This, will not be easy due to the progressive change in the thermal regime.

8 Bibliography

Anatoly O. Sinitsyn. (2020). *Impact of Climate Change on Infrastructure in Longyearbyen CASE STUDY OF PILE FOUNDATIONS ON SLOPING TERRAINS*. https://doi.org/10.13140/RG.2.2.33278.33601

European Environment Agency. (2017, June 15). *Permafrost in the Northern hemisphere*. https://www.eea.europa.eu/data-and-maps/figures/permafrost-in-the-northern-hemisphere

GeoStudio. (n.d.). Retrieved September 7, 2023, from https://www.geoslope.com/products/temp-w/features

Hanssen-Bauer, I., Førland, E. J., Hisdal, H., Mayer, S., Sandø, A. B., Sorteberg, A., Adakudlu, M., Andresen, J., Bakke, J., Beldring, S., Benestad, R., Bilt, W., Bogen, J., Borstad, C., Breili, K., Breivik, Ø., Børsheim, K. Y., Christiansen, H. H., Dobler, A., … Wong, W. K. (2018). *Climate in Svalbard 2100 Editors-a knowledge base for climate adaptation Title: Date*. http://www.miljodirektoratet.no/M1242

Heller, S. T. (2021). *A Numerical Simulation of Permafrost Thermal Regime under a Heat Pump Chilled Foundation in Longyearbyen, Svalbard*.

Huang, H.-C. (2020). *Experimental study on creep of frozen marine fine-grained soil in Longyearbyen, Svalbard*.

Instanes, A. (2016). Incorporating climate warming scenarios in coastal permafrost engineering design – Case studies from Svalbard and northwest Russia. *Cold Regions Science and Technology*, *131*, 76–87. https://doi.org/10.1016/j.coldregions.2016.09.004

Instanes, A., & Rongved, J. L. (2019). Climate change and geotechnical design in permafrost and frozen ground. *17th European Conference on Soil Mechanics and Geotechnical Engineering, ECSMGE 2019 - Proceedings*, *2019-September*. https://doi.org/10.32075/17ECSMGE-2019-0676

Instans Arne. (2017). *Coastal permafrost-foundation design Incorporating climate warming scenarios*.

Isaksen, K., Nordli, Ø., Ivanov, B., Køltzow, M. A. Ø., Aaboe, S., Gjelten, H. M., Mezghani, A., Eastwood, S., Førland, E., Benestad, R. E., Hanssen-Bauer, I., Brækkan, R., Sviashchennikov, P., Demin, V., Revina, A., & Karandasheva, T. (2022). Exceptional

warming over the Barents area. *Scientific Reports*, *12*(1). https://doi.org/10.1038/s41598-022-13568-5

Jean-Lous Briaud. (2013). *Geotechnical Engineering* (John Wiley & Sons, Ed.).

Kathrine Nitter. (2022). *Our arctic heritage is threatened by climate change - SINTEF*. https://www.sintef.no/en/latest-news/2022/our-arctic-heritage-is-threatened-by-climate-change/

Kristin Enevoldsen. (2022). *Rehabilitation of Cableway Posts, Longyearbyen*.

L. Gilbert, G., Instanes, A., O. Sinitsyn, A., & Aalberg, A. (2019). Characterization of two sites for geotechnical testing in permafrost: Longyearbyen, Svalbard. *AIMS Geosciences*, *5*(4), 868–885. https://doi.org/10.3934/geosci.2019.4.868

Mitchell, J. K. (James K., & Soga, K. (2005). *Fundamentals of soil behavior*.

Nybo, M. S., & Grimstad, G. (2017). *An experimental study of unfrozen water content in fine grained permafrost soils*.

Orlando B. Andersland, B. L. (2003). *Frozen Ground Engineering* (The Amerian Society of Civil Engineers & Inc. Wiley John & Sons, Eds.; Second Edition).

Rouyet, L., Lauknes, T. R., Christiansen, H. H., Strand, S. M., & Larsen, Y. (2019). Seasonal dynamics of a permafrost landscape, Adventdalen, Svalbard, investigated by InSAR. *Remote Sensing of Environment*, *231*. https://doi.org/10.1016/j.rse.2019.111236

Shastri, A., Sánchez, M., Gai, X., Lee, M. Y., & Dewers, T. (2021). Mechanical behavior of frozen soils: Experimental investigation and numerical modeling. *Computers and Geotechnics*, *138*. https://doi.org/10.1016/j.compgeo.2021.104361

Sinitsyn, A. O., Depina, I., Bekele, Y., Christensen, S., Dirk Van Oosterhout, •, & Research, S. (2020). *Development of coastal infrastructure in cold climate Summary Guideline SFI SAMCoT REPORT*. www.sintef.no/community

Van Everdingen, R. O. (1998). *MULTI-LANGUAGE GLOSSARY of PERMAFROST and RELATED GROUND-ICE TERMS*.

Zhang, H., Zhang, J., Zhang, Z., Zhang, M., & Cao, W. (2020). Variation behavior of pore-water pressure in warm frozen soil under load and its relation to deformation. *Acta Geotechnica*, *15*(3), 603–614. https://doi.org/10.1007/s11440-018-0736-4

Zhang, Y., Qian, Z., Lv, S., Huang, W., Ren, J., Fang, Z., & Chen, X. (2022). Experimental Investigation of Uniaxial Compressive Strength of Distilled Water Ice at Different Growth Temperatures. *Water (Switzerland)*, *14*(24). https://doi.org/10.3390/w14244079

9 Appendix A

As part of this research, a differential GPS (dGPS), see Figure 9.1, was employed to investigate select structures associated with the Longyearbyen post cableway. This instrument was used to measure the vertical heights at specific points on these structures. The objective of these measurements is to establish a baseline for future comparisons, tracking any potential changes in elevation over time.

The execution of this measurement process was conducted with meticulous care. It encompassed various stages, starting with the calibration of the DGPS device itself. Detailed records were maintained for each point where measurements were taken, complete with accompanying notes, sketches, and photographs. This comprehensive documentation process ensured the accuracy and repeatability of the measurements.

To further facilitate the replication of these measurements in the future, PowerPoint files were generated to provide precise guidance, see Figure 9.3.

The included image (Figure 9.2) depicts a map of Longyearbyen and its surrounding areas, highlighting all the structures that underwent investigation as part of this study.

Figure 9.1 Leica dGPS used to survey the cableway post structures durinf fieldwprk.

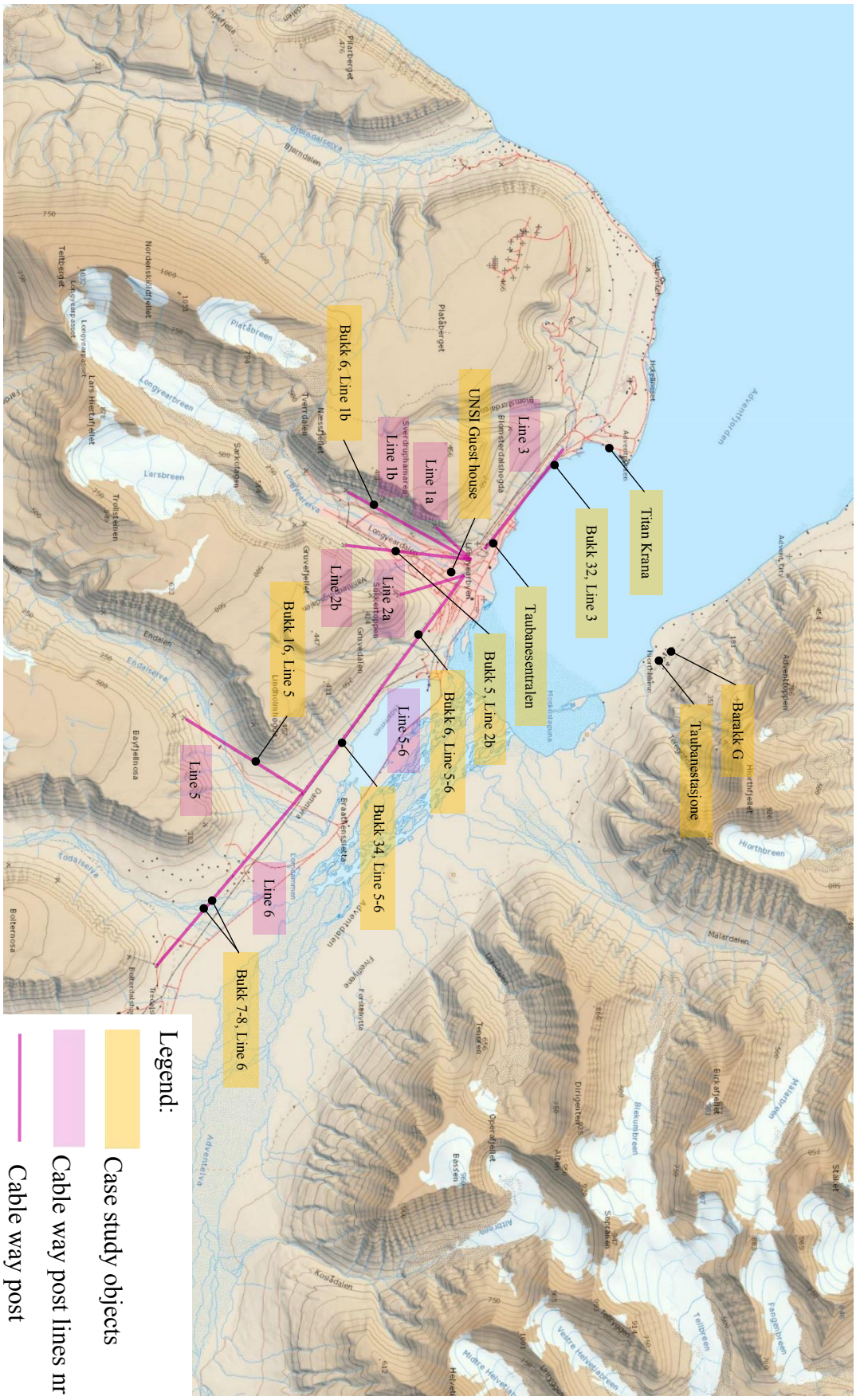

Figure 9.2 Map of the surveid structures in Longyearbyen and surroundings

Date	GPST	Lat	Lon	Height (m)	Standard deviation Height (m)	point
Bukk 7 Line 2b						
15.03.2023	11:18	78,13,08,32	15,385433	59,8132	0,0811	1 - 0002
15.03.2023	11:20:52	78,130826	15,385471	60,9391	0,0831	2 -0003
15.03.2023	11:23:16	78,13082	15,385517	60,3506	0,0808	3 - 0004
15.03.2023	11:25:58	78,130803	15,38547	60,9994	0,0792	4 - 0005
15.03.2023	11:28:13	78,130809	15,385427	60,845	0,1039	5 - 0006
15.03.2023	11:30:18	78,130816	15,385373	60,2288	0,0767	6 - 0007
Titan Krana						
17.03.2023	09:54:04	78,144885	15,324069	35,9018	0,1804	1.1 - 0008
17.03.2023	09:56:53	78,14488	15,324065	35,211	0,1528	1.2 - 0009
17.03.2023	10:15:59	78,144885	15,324053	32,8433	0,1794	1.3 - 0012
17.03.2023	10:18:07	78,144886	15,32403	34,0227	0,1757	1.4 - 0013
17.03.2023	10:26:01	78,144837	15,323981	39,4874	0,1711	2.1 - 0015
17.03.2023	10:28:07	78,144837	15,323977	38,9368	0,173	2.2 - 0016
17.03.2023	10:35:02	78,144833	15,323962	35,3956	0,1721	2.3 - 0017
17.03.2023	10:37:13	78,144834	15,323948	34,3118	0,1503	2.4 - 0018
17.03.2023	10:50:11	78,144949	15,323091	36,0701	0,1236	3.1 - 0019
17.03.2023	10:52:20	78,144948	15,323097	36,8448	0,1213	3.2 - 0020
17.03.2023	10:54:38	78,144951	15,323067	35,707	0,1167	3.3 - 0021
17.03.2023	10:56:56	78,144951	15,32364	36,0396	0,1248	3.4 - 0022
17.03.2023	11:07:12	78,144903	15,323002	37,5444	0,1494	4.1 - 0023
17.03.2023	11:09:48	78,1449	15,323008	37,4684	0,1522	4.2 - 0024
17.03.2023	11:12:18	78,144906	15,32299	36,0477	0,1425	4.3 - 0025
17.03.2023	11:14:21	78,144908	15,322973	39,0398	0,152	4.4 - 0026
Taubanestasjonen						
17.03.2023	14:25:51	78,134377	15,235032	34,4529	0,0914	1 - 0002
17.03.2023	14:27:58	78,145446	15,420362	33,3683	0,0807	2 - 0003
17.03.2023	14:30:41	78,145444	15,420348	34,8309	0,0669	3 - 0004
17.03.2023	14:32:35	78,145445	15,420359	34,2019	0,0656	4 - 0005
17.03.2023	14:34:51	78,145457	15,420359	33,7444	0,0553	5 - 0006
17.03.2023	14:37:01	78,145456	15,42036	33,3127	0,1068	6 - 0007
17.03.2023	14:40:45	78,145446	15,420419	33,4781	0,0456	7 - 0008
17.03.2023	14:42:50	78,145445	15,420413	34,2063	0,0438	8 - 0009
17.03.2023	14:51:07	78,145421	15,420315	33,8994	0,0617	9 - 0010
17.03.2023	14:53:18	78,145436	15,420246	35,6186	0,0265	10 - 0011
17.03.2023	14:58:02	78,145419	15,420143	32,7992	0,1333	11 - 0012
17.03.2023	15:00:27	78,145402	15,420234	31,7276	0,0729	12 - 0013
Bukk 8 Line 6						
17.03.2023	15:46:22	78,104419	15,533978	61,1888	0,037	1 - 0001
17.03.2023	15:49:09	78,104437	15,53405	62,1707	0,0341	2 - 0002
17.03.2023	15:52:11	78,10443	15,534082	61,3497	0,0373	3 - 0003

17.03.2023	15:55:19	78,104414	15,53401	61,7207	0,0366	4 - 0004
Bukk 7 Line 6						
17.03.2023	16:06:11	78,104264	15,534869	61,9648	0,0099	1.1 - 0005
17.03.2023	16:07:40	78,104263	15,534869	61,6989	0,0336	1.2 - 0006
17.03.2023	16:11:17	78,10428	15,534932	61,9821	0,0277	2 - 0007
17.03.2023	16:13:52	78,104273	15,534977	61,5378	0,0295	3 - 0008
17.03.2023	16:16:57	78,104258	15,534917	61,5405	0,0235	4 - 0009
Bukk 16 Line 5						
17.03.2023	17:00:05	78,113305	15,465121	85,7296	0,0399	1 - 0010
17.03.2023	17:02:17	78,113301	15,465109	85,5555	0,0508	2 - 0011
17.03.2023	17:05:00	78,11329	15,465082	85,7092	0,0348	3 - 0012
17.03.2023	17:07:12	78,113301	15,464998	85,6946	0,0391	4 - 0013
17.03.2023	17:09:19	78,113305	15,465013	85,6836	0,0523	5 - 0014
17.03.2023	17:13:41	78,13314	15,465035	88,60481	0,0399	6 - 0016
Bukk 6 Line 2b						
18.03.2023	10:26:26	78,12353	15,365599	91,9959	0,0631	1 - 0001
18.03.2023	10:30:46	78,123526	15,5693	92,1747	0,0512	2 - 0002
18.03.2023	10:33:47	78,123503	15,365671	91,646	0,0084	3 - 0003
18.03.2023	10:37:22	78,123506	15,36558	92,2969	0,0562	4 - 0004
18.03.2023	10:50:13	78,122846	15,365086	125,0853	0,0706	1 - 0005
18.03.2023	10:54:56	78,122838	15,365065	127,0056	0,146	2 - 0006
18.03.2023	10:57:33	78,122835	15,365065	126,7203	0,128	3 - 0007
18.03.2023	11:13:47	78,122493	15,364893	148,1395	0,1012	1 - 0008
18.03.2023	11:18:13	78,12248	15,36488	148,6771	0,1102	2 - 0009
18.03.2023	11:23:45	78,122486	15	149,619	0,1028	3 - 0010
18.03.2023	11:29:31	78,122495	15,36481	149,0424	0,094	4 - 0011
Bukk 6 Line 1b						
18.03.2023	12:10:26	78,123128	15,345554	183,4267	0,0846	1 - 0012
18.03.2023	12:14:18	78,12312	15,345533	182,5999	0,1014	2 - 0013
18.03.2023	12:18:01	78,123126	15,345542	183,646	0,0744	3 - 0014
Taubanesentralen						
18.03.2023	14:29:16	78,132437	15,36568	95,1062	0,1416	1 - 0015
18.03.2023	14:32:04	78,132431	15,3658	93,5519	0,1468	2 - 0016
18.03.2023	14:35:41	78,132435	15,370145	89,3677	0,1567	3 -0017
18.03.2023	14:37:52	78,132429	15,37018	92,0328	0,1821	1 - 0018
18.03.2023	14:42:12	78,132393	15,370241	87,0356	0,0401	2 - 0019
18.03.2023	14:44:52	78,132393	15,370244	87,7715	0,0662	3 - 0020
18.03.2023	14:48:33	78,132403	15,370343	86,2439	0,0599	4 - 0021
18.03.2023	14:53:19	78,132493	15,370276	85,5071	0,1798	5 -0022
18.03.2023	14:56:08	78,132447	15,370249	86,8866	0,2168	6 - 0023
18.03.2023	14:58:54	78,1325	15,370306	97,1961	0,4271	7 - 0024
18.03.2023	15:02:13	78,132472	15,370482	83,0617	0,0727	8 - 0025
18.03.2023	15:04:11	78,132472	15,235032	84,7021	0,0597	9 - 0026
18.03.2023	15:07:38	78,134377	15,23054	83,3455	0,019	10 - 0027

18.03.2023	15:09:23	78,132489	15,370541	83,6449	0,0527	11 - 0028
18.03.2023	15:12:14	78,132511	15,370398	80,2005	0,2098	12 - 0029
18.03.2023	15:14:16	78,132512	15,370398	83,7258	0,189	13 - 0030
18.03.2023	15:21:14	78,132549	15,365554	95,8781	0,2086	1 - 0031
Bukk 23 Line 1b - Restored						
18.03.2023	15:31:35	78,131907	15,364472	112,208	0,0572	1 - 0032
18.03.2023	15:34:00	78,131892	15,364438	112,3913	0,0492	2 - 0033
18.03.2023	15:36:40	78,131885	15,364524	112,8011	0,0026	3 - 0034
18.03.2023	15:40:45	78,131899	15,364563	111,9853	0,052	4 - 0035
Bukk 3 Line 5-6						
18.03.2023	15:54:32	78,131898	15,374415	63,3174	0,0019	1 - 0036
18.03.2023	15:57:05	78,131885	15,374501	63,3263	0,0077	2 - 0037
18.03.2023	16:00:32	78,13187	15,374451	63,2605	0,0019	3 - 0038
18.03.2023	16:02:59	78,131883	15,374362	62,9302	0,0381	4 - 0039
Bukk 4 Line 5-6						
18.03.2023	16:10:11	78,131571	15,380567	48,5716	0,0067	1 - 0040
18.03.2023	16:12:40	78,131555	15,380503	48,671	0,0471	2 - 0041
18.03.2023	16:15:10	78,131536	15,380625	47,3619	0,0093	3 - 0042
18.03.2023	16:17:42	78,131553	15,380683	48,6543	0,0496	4 - 0043
Bukk 34 Line 5-6						
13.04.2023	10:30:11	78,121407	15,444992	61,129	0,076	1 - 0001
13.04.2023	10:33:13	78,121393	15,444938	61,76	0,002	2 - 0002
13.04.2023	10:36:49	78,121397	15,444918	62,493	0,06	3 - 0003
13.04.2023	10:39:57	78,121398	15,4449	60,945	0,06	4 - 0004
13.04.2023	10:42:26	78,1214	15,444884	61,648	0,057	5 - 0005
13.04.2023	10:45:36	78,121415	15,444936	61,097	0,046	6 - 0006
Bukk 32 Line 3						
13.04.2023	11:37:00	78,140256	15,331722	59,949	0,002	1 - 0001
13.04.2023	11:39:36	78,120262	15,33168	59,752	0,006	2 - 0002
13.04.2023	11:42:21	78,140276	15,331736	59,883	0,002	3 - 0003
13.04.2023	11:44:46	78,14027	15,331775	59,883	0,003	4 - 0004

Table 9.1 dGPS heights results after data postprocessing.

We currently lack comparative data for the recently acquired with our measurements, as this marks the initial phase of our study. The objective is to subsequently conduct additional measurements to further understand the extent of settlement in the foundations of the selected structures.

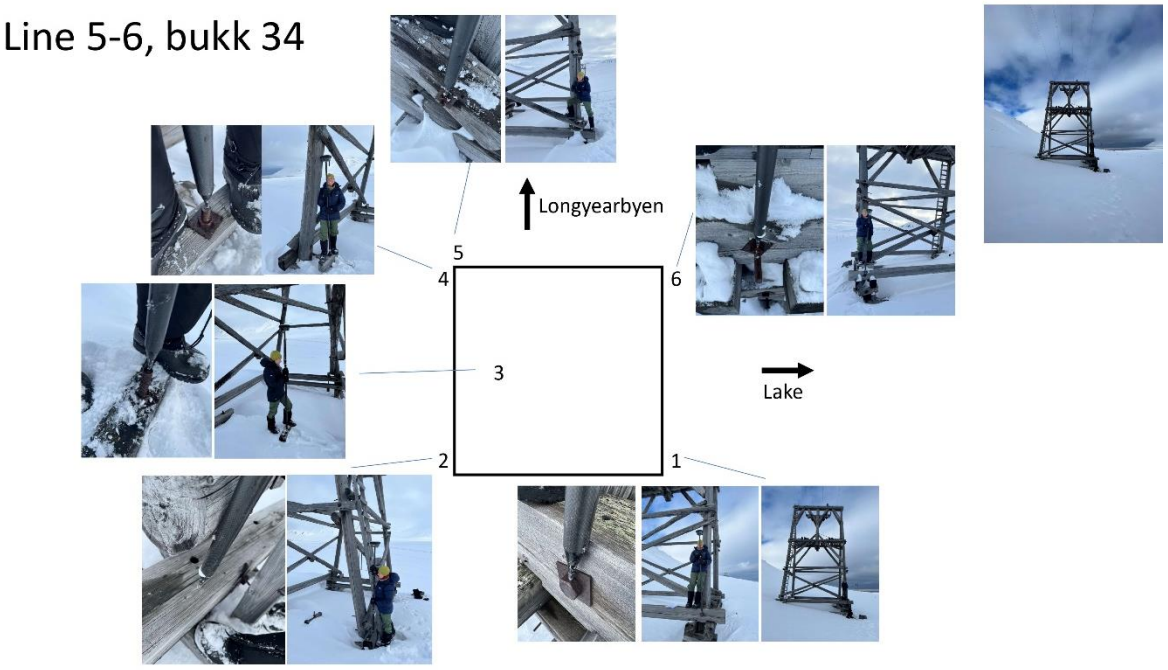

Figure 9.3 PowerPoint slide example.

Figure 9.4 Pictures from fieldwork in April 2023, with Anatoly Sinitsyn and Anni Vehola.

10 Appendix B

A part of the Arctic Field Grant (AFG) was allocated to support fieldwork conducted using a Laser Level in both Longyearbyen and Ny-Ålesund. This device was utilized to determine the settlement of building foundations, including the still-in-use UNIS Guest House in Longyearbyen and several historically significant structures in Ny-Ålesund, see Figure 10.3.

Figure 10.1 Longyearbyen, 78 degree North and Ny- Ålesund research settlement, 79 degrees North. Fieldwork locations.

In the map below, Figure 10.2, the locations of the buildings investigated in Ny-Ålesund have been marked. The execution of this task demanded precision and thorough planning at every stage to ensure the replicability of the process in subsequent years.

Figure 10.2 Map of the surveid buildings in Ny-Ålesund.

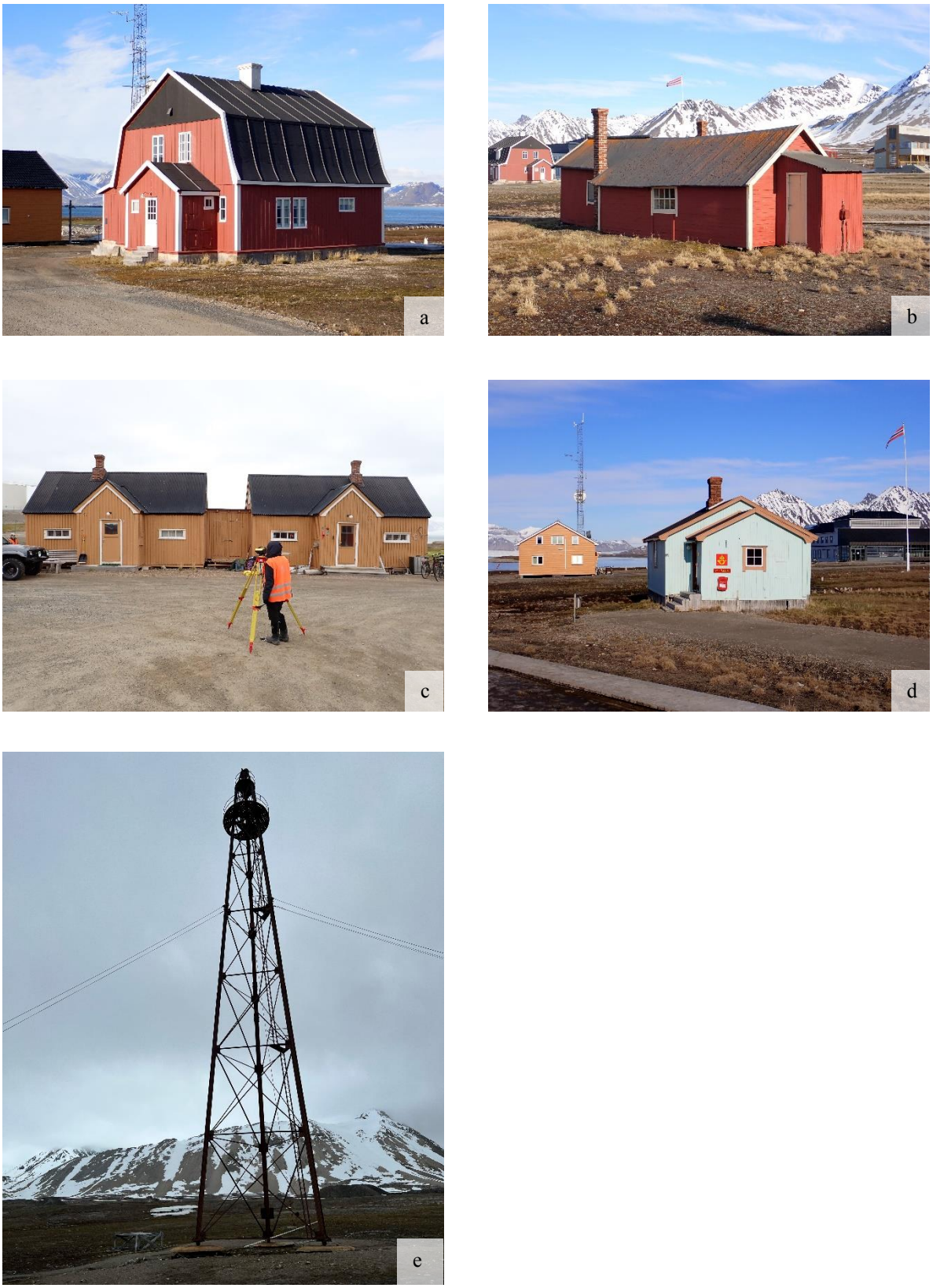

Figure 10.3 (a) Amundsen Villa, (b) Green Harbour House, (c) London Houses, (d) Post office (with reference to official bench mark in Ny-Ålesund); (e) Luftskipsmasta (with reference to newly installed on a pile embedded in the bedrock next to it).

The following maps, see Figure 10.4 and Figure 10.5, illustrate the routes followed, highlighting the selection of base points and intermediate locations for data collection purposes.

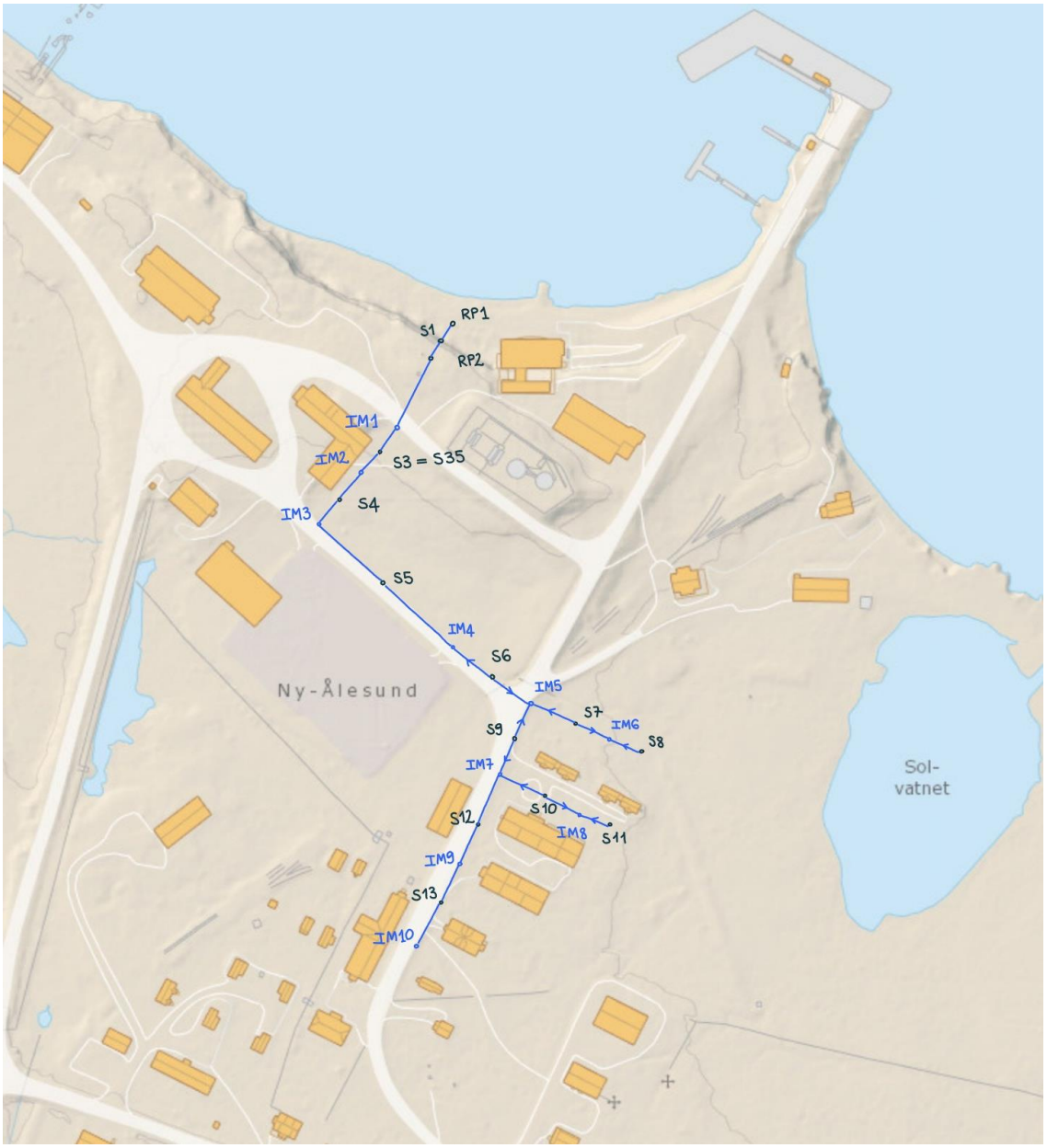

Figure 10.4 Map of Stations and Intermediate Points: from Reference Point 1 to Station 13.

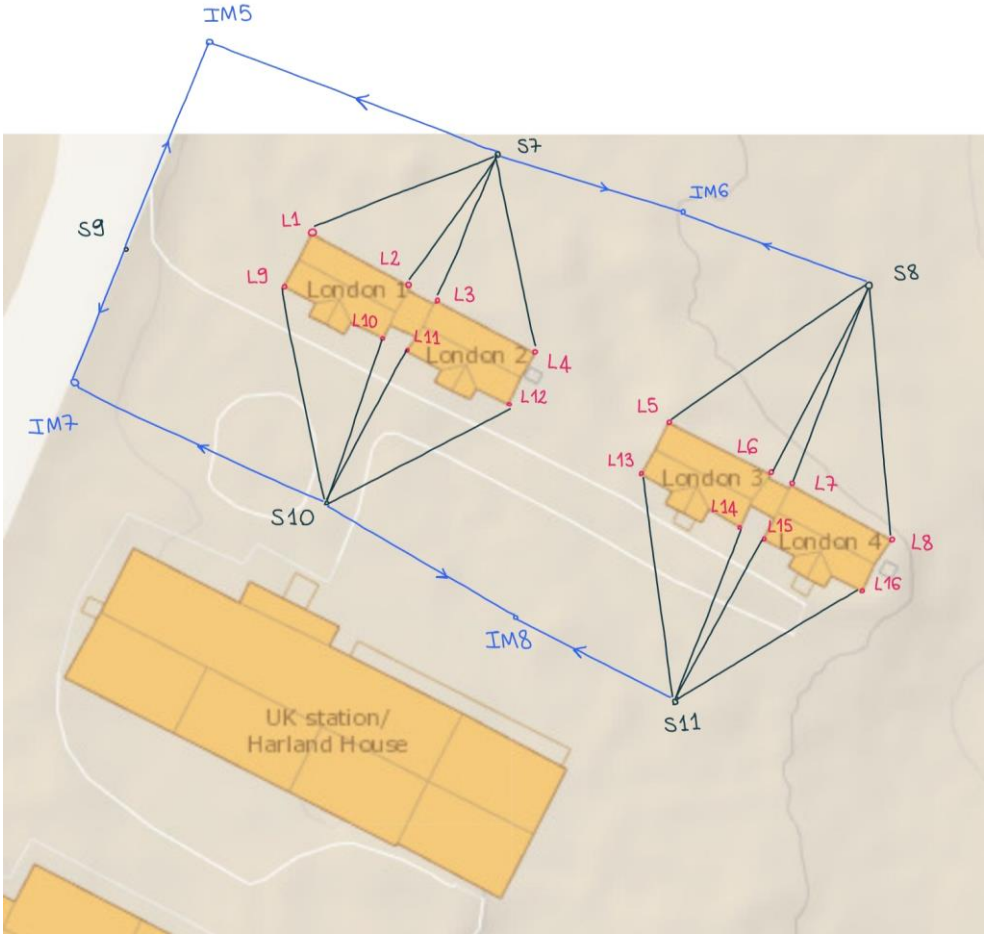

Figure 10.5 Map of the points used to survey the London Houses (used as an example, the same has been done on the other buildings with attached photos of each point).

For the UNIS Guest House, we possessed data from previous years, dating back to 2018 and 2019, which enabled us to perform comparisons regarding foundation settlement.

Regarding the buildings in Ny-Ålesund, there were no previous measurements available. Nevertheless, initial observations, both from field investigations and the measurements taken, indicated some noticeable subsidence in these structures, see Figure 10.6 and Figure 10.7.

Figure 10.6 Green Harbour House settlement of ca. 15 cm already visible from field investigation. Wooden foundations decay must be expected.

Figure 10.7 London Houses settlement of ca. 12 cm already visible from field investigation.

Figure 10.8 Luftskipsmasta, visible permafrost degradation under the foundation concrete place.

Figure 10.9 Anni Vehola and I surveing Luftskipsmasta with the Laser level. Picture taken by Anatoly Sinitsyn, helping us during the fieldwok.

Figure 10.10 Anatoly Sinitsyn, Anni Vehola and I surveing the Post Office building in Ny-Ålesund.